NASA/TM—2011-216970

Gas Flux and Density Surrounding a Cylindrical Aperture in the Free Molecular Flow Regime

George C. Soulas
Glenn Research Center, Cleveland, Ohio

March 2011

NASA STI Program . . . in Profile

Since its founding, NASA has been dedicated to the advancement of aeronautics and space science. The NASA Scientific and Technical Information (STI) program plays a key part in helping NASA maintain this important role.

The NASA STI Program operates under the auspices of the Agency Chief Information Officer. It collects, organizes, provides for archiving, and disseminates NASA's STI. The NASA STI program provides access to the NASA Aeronautics and Space Database and its public interface, the NASA Technical Reports Server, thus providing one of the largest collections of aeronautical and space science STI in the world. Results are published in both non-NASA channels and by NASA in the NASA STI Report Series, which includes the following report types:

- TECHNICAL PUBLICATION. Reports of completed research or a major significant phase of research that present the results of NASA programs and include extensive data or theoretical analysis. Includes compilations of significant scientific and technical data and information deemed to be of continuing reference value. NASA counterpart of peer-reviewed formal professional papers but has less stringent limitations on manuscript length and extent of graphic presentations.

- TECHNICAL MEMORANDUM. Scientific and technical findings that are preliminary or of specialized interest, e.g., quick release reports, working papers, and bibliographies that contain minimal annotation. Does not contain extensive analysis.

- CONTRACTOR REPORT. Scientific and technical findings by NASA-sponsored contractors and grantees.

- CONFERENCE PUBLICATION. Collected papers from scientific and technical conferences, symposia, seminars, or other meetings sponsored or cosponsored by NASA.

- SPECIAL PUBLICATION. Scientific, technical, or historical information from NASA programs, projects, and missions, often concerned with subjects having substantial public interest.

- TECHNICAL TRANSLATION. English-language translations of foreign scientific and technical material pertinent to NASA's mission.

Specialized services also include creating custom thesauri, building customized databases, organizing and publishing research results.

For more information about the NASA STI program, see the following:

- Access the NASA STI program home page at *http://www.sti.nasa.gov*

- E-mail your question via the Internet to *help@sti.nasa.gov*

- Fax your question to the NASA STI Help Desk at 443–757–5803

- Telephone the NASA STI Help Desk at 443–757–5802

- Write to:
  NASA Center for AeroSpace Information (CASI)
  7115 Standard Drive
  Hanover, MD 21076–1320
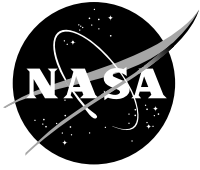
Gas Flux and Density Surrounding a Cylindrical Aperture in the Free Molecular Flow Regime

George C. Soulas
Glenn Research Center, Cleveland, Ohio

Level of Review: This material has been technically reviewed by technical management.

Gas Flux and Density Surrounding a Cylindrical Aperture in the Free Molecular Flow Regime

George C. Soulas
National Aeronautics and Space Administration
Glenn Research Center
Cleveland, Ohio 44135

Abstract

The equations for rigorously calculating the particle flux and density surrounding a cylindrical aperture in the free molecular flow regime are developed and presented. The fundamental equations for particle flux and density from a reservoir and a diffusely reflecting surface will initially be developed. Assumptions will include a Maxwell-Boltzmann speed distribution, equal particle and wall temperatures, and a linear flux distribution along the cylindrical aperture walls. With this information, the equations for axial flux and density surrounding a cylindrical aperture will be developed. The cylindrical aperture will be divided into multiple volumes and regions to rigorously determine the surrounding axial flux and density, and appropriate limits of integration will be determined. The results of these equations will then be evaluated. The linear wall flux distribution assumption will be assessed. The axial flux and density surrounding a cylindrical aperture with a thickness-to-radius ratio of 1.25 will be presented. Finally, the equations determined in this study will be verified using multiple methods.

Nomenclature

a	y-intercept in non-dimensional wall flux equation
A	area
b	slope in non-dimensional wall flux equation
c	mean thermal speed of particles within the reservoir
$f(v)$	Maxwell-Boltzmann space speed distribution function
n	particle density
L	distance between the surface normals of dA_o and dA_c
$\dot{N}$	particle flow rate
P	particle transmission probability through a cylindrical aperture
R	aperture radius
R_p	projected circle radius
r	radial location
r_{oII}	radial limit of integration for the reservoir's contribution to the downstream flux and density
r_{oIII}	radial limit of integration for the reservoir's contribution to the downstream flux and density
t	aperture plate thickness
T	far-field angular distribution function for particles downstream of a cylindrical aperture
v	particle speed
z	axial location
z_{wII}	axial limit of integration for the wall's contribution to the downstream flux and density
z_{wIIn}	axial limit of integration for the wall's contribution to the upstream flux and density

Greek Symbols:

α	angle from dA_o surface normal to L
β	angle

γ	angle
Γ	particle flux
$\hat{\Gamma}_o$	reservoir or wall flux per steradian
δ	angle from dA_c surface normal to L
θ	polar angle in a spherical coordinate system
κ	far-field angular distribution function variable
φ	azimuthal angle
φ_{omax}	angular limit of integration for the reservoir's contribution to the downstream flux and density
φ_{oII}	angular limit of integration for the reservoir's contribution to the downstream flux and density
φ_{wII}	angular limit of integration for the wall's contribution to the downstream flux and density
φ_{wIIn}	angular limit of integration for the wall's contribution to the upstream flux and density
φ_{wt}	angular limit of integration for the wall's contribution to the flux and density
ω	solid angle

Subscripts and Superscripts:

-	non-dimensionalized value (dimensions are divided by R, densities by n_o, and fluxes by Γ_o)
c	collection site
f	final location for the limit of integration
far	far-field variable
i	initial location for the limit of integration
o	reservoir
up	upstream reservoir
w	aperture wall

I. Introduction

Accurately predicting the density and flux of particles emanating from a circular aperture of finite thickness (i.e., a cylindrical aperture) is of significant interest for ion thrusters. Ion thrusters create ions within a discharge chamber and accelerate these ions through perforated grids composed of thousands of cylindrical apertures to produce thrust (Refs. 1 and 2). Xenon is the propellant used for present spacecraft ion thruster applications. One consequence of beam ion generation is that unionized gas can escape from the thruster discharge chamber through the cylindrical apertures of the grids. Predicting the downstream unionized gas density distribution is important for determining its impact on the thruster and surrounding spacecraft environment. For example, slow-moving ions are created with beam ions and the escaping unionized gas due to a process known as charge-exchange. These slow-moving ions can either impact the thruster's accelerator grid, causing erosion and limiting thruster service life, or they can impact spacecraft surfaces.

Ion thrusters operate at neutral densities that are so low that particles travel from surface to surface without colliding. For example, the neutral-to-neutral mean free paths are greater than 34 cm within a state-of-the-art discharge chamber, which is greater than the radius of the chamber (Ref. 3). This rarified gas flow regime is often referred to as free molecular flow. Solving for the downstream particle density distribution requires an understanding of how the thickness of a cylindrical aperture can affect this downstream distribution.

Many ion thrusters utilize two grids to accelerate ions, and these include an upstream screen grid and a downstream accelerator grid. So, for a unionized gas to escape the discharge chamber, it must travel through two apertures, which presents a difficult problem to solve. Fortunately, though, the upstream screen grid aperture is typically much larger and thinner than the accelerator grid aperture. As a result, the angular distribution of particles exiting the accelerator aperture is well modeled by assuming a single accelerator aperture (Ref. 3).

Many past studies have considered this problem of the free molecular flow through a cylindrical aperture. Clausing was the first to determine the downstream angular distribution pattern of particles emanating from a thin cylindrical tube under free molecular flow conditions (Refs. 4 and 5). However, his distribution equation was only

appropriate for far-field calculations of particle fluxes and densities, as explained by Reynolds and Richley (Ref. 6). Richley and Reynolds determined the flux of particles within converging and diverging cylindrical tubes (Refs. 6 and 7). And Robertson conducted similar studies to determine particle densities as well (Ref. 8). The results of both investigations can be extended axially downstream of the cylindrical aperture to determine near- and far-field densities and fluxes. Unfortunately, the resulting equations are not accurate at radial locations greater than the radius of the aperture, which imposes a severe limitation on their use. Another method of determining particle density and flux distributions is to use a Monte Carlo simulation technique (Ref. 9). Such a technique allows for the quick analysis of complex geometries (see, for example, Ref. 10). However, accurately analyzing downstream regions where particle densities and fluxes have decreased significantly is computationally difficult. In addition, this technique does not lend itself well to ion thruster grids which have thousands of cylindrical apertures.

In this study, equations will be developed for rigorously calculating the flux and density of particles surrounding a cylindrical aperture in the free molecular flow regime. The fundamental equations and their assumptions necessary to determine particle densities and fluxes will be presented first. These equations will then be applied to a cylindrical aperture to determine the particle flux distribution from the cylindrical aperture walls. With this information, the equations for particle density and flux surrounding a cylindrical aperture will be developed. Finally, the resulting equations will be applied to a typical ion thruster aperture and compared to that of Clausing in the far-field (Ref. 4).

II. Fundamental Equations for Particle Flux and Density

The particle flux and density distributions surrounding a cylindrical aperture were determined using the following assumptions:

1. Particles upstream of a cylindrical aperture reside within a reservoir and exhaust into a vacuum through the cylindrical aperture;
2. Equilibrium conditions exist, so that the rate of particles leaving the reservoir is equal to the rate of particles fed into the reservoir;
3. The particle density is sufficiently low that free molecular flow conditions exist within the aperture;
4. All wall reflections are diffuse;
5. Particle adsorption onto the walls and surface diffusion are negligible;
6. Wall temperatures are equal to the particle temperature; and
7. Particles within the reservoir have a Maxwell-Boltzmann speed distribution.

The geometric relation between a differential element from a particle emission site (i.e., a wall or the upstream reservoir) and a differential element from a downstream collection site is shown in Figure 1.
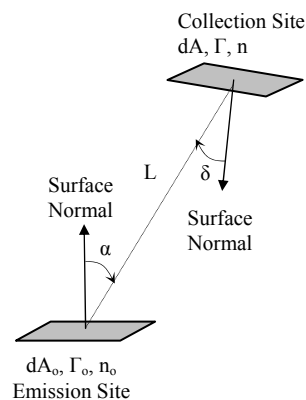

Figure 1.—Geometric relation between a particle emission site and the downstream collection site.

The variable α is the angle between the surface normal of the emission site to the collecting site's differential surface area, dA, and δ is the angle between the surface normal of dA to the differential emitting area, dA_o. The variable L is the distance between the emitting and collecting differential areas. The particle flow rate, $\dot{N}$, from a differential emission area to a downstream differential collection area is given by:

$$d^2\dot{N} = \hat{\Gamma}_o(A_o) \cdot dA_o \cdot \cos(\alpha) \cdot d\omega \qquad (1)$$

Here, $\hat{\Gamma}_o$ is the emitted particle flux per steradian from differential area dA_o and is a function of A_o. The downstream solid angle, $d\omega$, is given by:

$$d\omega = \frac{dA \cdot \cos(\delta)}{L^2} \qquad (2)$$

By substituting Equation (2) into Equation (1) and dividing both sides by dA, the following equation is obtained:

$$d\left(\frac{\dot{N}}{dA}\right) = d\Gamma = \hat{\Gamma}_o(A_o) \cdot \frac{\cos(\alpha) \cdot \cos(\delta)}{L^2} \cdot dA_o \qquad (3)$$

Here, Γ is the flux to the collection site. The emitted particle flux, Γ_o, can be evaluated as a function of the emitted particle flux per steradian by noting that for diffuse surface emission, $\hat{\Gamma}_o$ is independent of emission angle, so that:

$$\Gamma_o = \int_0^{2\cdot\pi} \int_0^{\frac{\pi}{2}} \hat{\Gamma}_o \cdot \cos(\theta) \cdot \sin(\theta) \cdot d\theta \cdot d\phi = \pi \cdot \hat{\Gamma}_o \qquad (4)$$

Note that particles from the upstream reservoir and reflected from a wall can both be assumed to be leave differential area dA_o diffusely. Substituting this result into Equation (3) and integrating both sides yields our fundamental equation for particle fluxes:

$$\Gamma = \frac{1}{\pi} \cdot \int_{A_o} \Gamma_o(A_o) \cdot \frac{\cos(\alpha) \cdot \cos(\delta)}{L^2} \cdot dA_o \qquad (5)$$

Note that if the emission site is the reservoir, Γ_o is independent of A_o and equal to:

$$\Gamma_o = \frac{n_o \cdot c}{4} \qquad (6)$$

where c is the mean speed of the particles within the reservoir and n_o is the reservoir particle density.

The downstream particle density, n, from a reservoir of particles can be solved by starting with the Maxwell-Boltzmann phase space speed distribution function (Ref. 11). Because equilibrium conditions were assumed, the speed distribution function, f(v), is independent of position (i.e., particle velocity is isotropic). So, the particle density downstream of a reservoir is:

$$n = n_o \cdot \iiint_\infty f(v) \cdot d^3v = n_o \cdot \int_0^\infty \int_{\omega_o} f(v) \cdot d\omega_o \cdot dv = n_o \cdot \int_0^\infty f(v) \cdot dv \cdot \int_{\omega_o} \cdot d\omega_o \qquad (7)$$

Here, n_o is the particle density within the reservoir and the differential solid angle, $d\omega_o$, is given by:

$$d\omega_o = \frac{dA_o \cdot \cos(\alpha)}{L^2} \qquad (8)$$

The first integral on the right-hand side of Equation (7) can be shown to be $1/(4 \cdot \pi)$, so substituting this and Equation (8) into Equation (7) yields:

$$n = \frac{n_o}{4 \cdot \pi} \cdot \int_{A_o} \frac{\cos(\alpha)}{L^2} \cdot dA_o \tag{9}$$

This equation is in a form that is useful for solving for the downstream particle density when the emission site is the reservoir. When the emission site is a wall, it is more useful to re-express Equation (9) using a particle flux. This is done by solving Equation (6) for n_w and substituting this into Equation (7) to obtain:

$$n = \iiint_\infty \frac{4 \cdot \Gamma_w}{c} \cdot f(v) \cdot d^3 v = \int_0^\infty f(v) \cdot dv \cdot \int_{\omega_o} \frac{4 \cdot \Gamma_w}{c} \cdot d\omega_o \tag{10}$$

Note that Γ_w appears with the second integral because the wall flux will be shown to be a function of the location on the wall. Substituting Equation (8) into Equation (10) yields:

$$n = \frac{1}{c \cdot \pi} \cdot \int_{A_w} \Gamma_w(A_w) \cdot \frac{\cos(\alpha)}{L^2} \cdot dA_w \tag{11}$$

which is in a form that is useful for solving the particle density when a reflecting wall is the emission site.

III. Equation for the Particle Flux From the Aperture Walls

The particle fluxes and densities surrounding a cylindrical aperture are a function of particle fluxes from the reservoir and cylindrical aperture walls. While the particle flux from a reservoir is given by Equation (6), the wall flux has yet to be determined. The following section will review the development of the wall flux equation used in this study.

Figure 2 is a schematic of the cylindrical aperture and the coordinate system used in this study. A cylindrical coordinate system will be used for the cylindrical aperture of radius R and thickness t. Also illustrated in Figure 1 are the labels for the relevant surfaces and volumes. These labels will be used as subscripts within this study. It is convenient to non-dimensionalize the resulting equations, as was done in References 6 and 7. All dimensions will, therefore, be non-dimensionalized with the aperture radius, R, all particle fluxes will be non-dimensionalized with reservoir flux, Γ_o, and all particle densities will be non-dimensionalized with reservoir density, n_o. Non-dimensionalized values will be denoted with a bar above the variable throughout this paper.
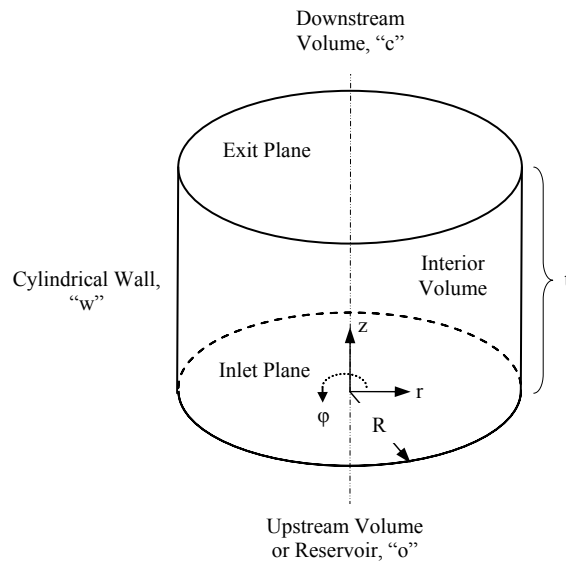

Figure 2.—Schematic of the cylindrical aperture for this investigation.

The particle flux to the aperture walls has been solved many times before in literature (see, for example, Refs. 6, 7, and 12). The following derivation can be found in References 6 and 7. The particle flux from the wall (i.e., surface "w") of the aperture consists of the particle flux from upstream reservoir (i.e., surface "o") arriving directly onto the wall and the particle flux from the other wall regions arriving back onto itself. Because of the symmetry of the problem, the particle flux from the wall is independent of φ. So, by applying Equation (5) to the reservoir and wall, the flux from the wall at any location z becomes:

$$\Gamma_w(z) = \frac{\Gamma_o}{\pi} \cdot \int_{A_o} \frac{\cos(\alpha_{o-w}) \cdot \cos(\delta_{w-o})}{L_{w-o}^2} \cdot dA_o + \frac{1}{\pi} \cdot \int_{A_w} \Gamma_w(z) \cdot \frac{\cos(\alpha_{w-w}) \cdot \cos(\delta_{w-w})}{L_{w-w}^2} \cdot dA_w \qquad (12)$$

Note here that a two digit subscript denotes two different surfaces. So, for example, L_{o-w} refers to the distance L between elemental areas on the wall and inlet plane (see Fig. 1).

To solve this equation, $\cos(\alpha)$, $\cos(\delta)$, L, and A for each integral must be solved as functions of z and the respective integral variable. The resulting solution in non-dimensional form is given by (Refs. 6 and 7):

$$\overline{\Gamma}_w(\overline{z}) = \frac{1}{2} \cdot \left[\frac{\overline{z}^2 + 2}{\sqrt{\overline{z}^2 + 4}} - \overline{z} \right] + \int_0^{\overline{t}} \frac{\overline{\Gamma}_w(\overline{z}_w)}{2} \cdot \left\{ 1 - |\overline{z}_w - \overline{z}| \cdot \frac{(\overline{z}_w - \overline{z})^2 + 6}{\left[(\overline{z}_w - \overline{z})^2 + 4 \right]^{\frac{3}{2}}} \right\} \cdot d\overline{z}_w \qquad (13)$$

This equation has the form of a Fredholm integral equation of the second kind. This integral equation was solved numerically using an algorithm identical to that described in Reference 7. The resulting non-dimensional particle fluxes from the aperture wall are plotted as a function of the normalized wall axial location for various aperture thickness-to-diameter ratios in Figure 3. The figure illustrates a critical characteristic of free molecular flow through an aperture: the particle flux from an aperture wall as a function of wall axial location is linear over a broad range aperture thickness-to-diameter ratios. Indeed, as the aperture thickness-to-radius decreases, the functional relation becomes more linear. Over the range of thickness-to-radius ratios examined by this author in Figure 3, a linear assumption accurately models the wall particle flux as a function of wall axial location. Other characteristics include:

1. The wall particle flux as a function of wall axial location has a negative slope. This is because the source of particles is the upstream reservoir.
2. The non-dimensional particle flux approaches 1 at the entrance and 0 at the exit as the thickness-to-radius ratio increases. Again, this is because the source of particles is the upstream reservoir.
3. Over the range of thickness-to-radius ratios examined, the non-dimensional wall particle flux was 1/2 at the middle of the wall.

Given the linear behavior of wall particle flux as a function of axial location, the integral equation of Equation (13) can be solved by assuming a linear equation for the solution. Clausing was the first to do this, and found the solution to be (Ref. 4):

$$\overline{\Gamma}_w(\overline{z}) = a + b \cdot \overline{z} \qquad (14)$$

where a and b are given by:

$$a = \frac{\left(\frac{\overline{t}}{2} + 1 \right) \cdot \sqrt{\overline{t}^2 + 4} - \frac{\overline{t}^2}{2}}{\sqrt{\overline{t}^2 + 4} + 2} \qquad (15)$$

and:

$$b = \frac{\overline{t}^2 + 2 - (\overline{t} + 1) \cdot \sqrt{\overline{t}^2 + 4}}{\overline{t} \cdot \left(\sqrt{\overline{t}^2 + 4} + 2 \right)} \qquad (16)$$
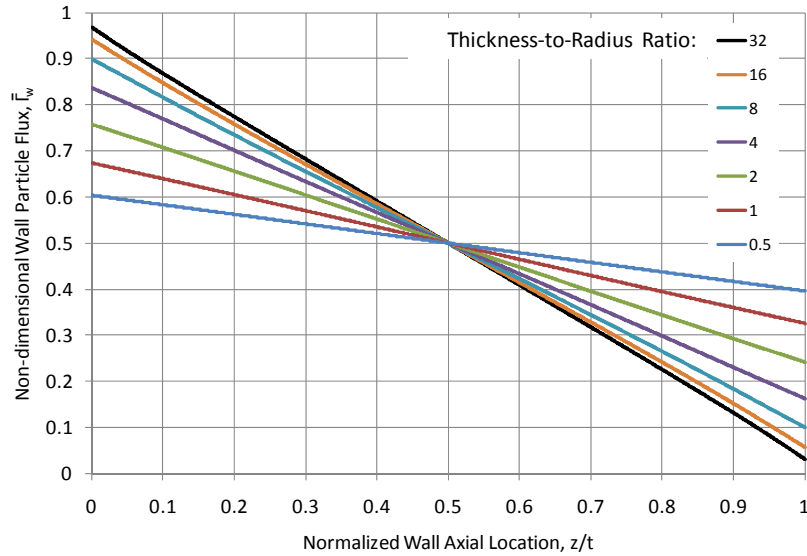
respectively.

Figure 3.—Non-dimensional particle flux from the aperture walls as a function of the normalized wall axial location for various aperture thickness-to-radius ratios. Aperture locations were normalized with the aperture thickness, t.
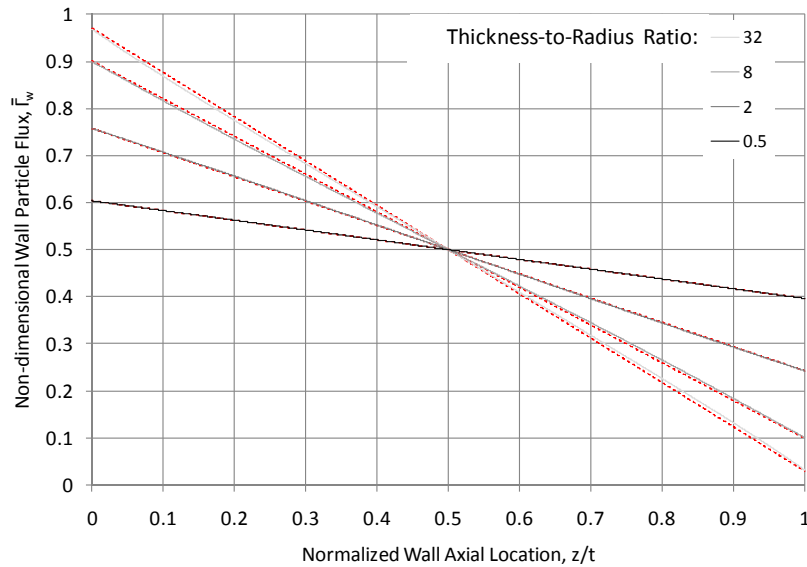

Figure 4.—Comparison particle fluxes from the aperture walls as a function of the normalized wall axial location for various aperture thickness-to-radius ratios. Solid lines are numerically-determined and the dotted red lines are the respective values determined assuming a linear distribution. The wall axial location was normalized to the aperture thickness, t.

Figure 4 compares the wall particle flux predicted by Equations (14) to (16) to that determined numerically. The worst-case difference between the two methods for aperture thickness-to-radius ratios up to 32 was less than 0.01 (in non-dimensional form).

The remainder of this study will therefore assume that the wall particle flux as a function of wall axial location is given by Equations (14) to (16) because the assumption used to develop these equations is valid over the aperture thickness-to-radius ratios of interest to ion thruster grids (i.e., an aperture thickness-to-radius ratio of ≤1.25). The efficacy of this linear assumption will be assessed later in the results section.

IV. Equations for the Particle Flux and Densities Surrounding a Cylindrical Aperture

In this section, the equations for determining particle fluxes and densities surrounding a cylindrical aperture will be determined. The first section develops the base equations. The second section divides the surrounding aperture in volumes, some of which are further divided into separate regions, and develops the limits of integration for these different cases. The last section presents the final equations for particle flux and density, as well as the transmission probability.

A. Development of the Base Equations for Particle Flux and Density Surrounding a Cylindrical Aperture

In this section, the base equations for determining the flux and density surrounding a cylindrical aperture are determined. Particle fluxes and densities surrounding an aperture are made up of contributions from the upstream reservoir and the aperture walls. Using Equation (5), the flux surrounding an aperture can be shown to be given by:

$$\Gamma = \frac{1}{\pi} \cdot \left\{ \Gamma_o \cdot \int_{A_o} \frac{\cos(\alpha_{o-c}) \cdot \cos(\delta_{o-c})}{L_{o-c}^2} \cdot dA_o + \int_{A_w} \Gamma_w(A_w) \cdot \frac{\cos(\alpha_{w-c}) \cdot \cos(\delta_{w-c})}{L_{w-c}^2} \cdot dA_w \right\} \tag{17}$$

Likewise, using Equations (9) and (11), the density surrounding an aperture can be shown to be given by:

$$n = \frac{1}{\pi} \cdot \left\{ \frac{n_o}{4} \cdot \int_{A_o} \frac{\cos(\alpha_{o-c})}{L_{o-c}^2} \cdot dA_o + \frac{1}{c} \cdot \int_{A_w} \Gamma_w(A_w) \cdot \frac{\cos(\alpha_{w-c})}{L_{w-c}^2} \cdot dA_w \right\} \tag{18}$$

Figure 5 shows a sketch of the geometric variables used in the equations above. For both equations, the left-hand integral is the reservoir's contribution while the right-hand is the aperture wall's contribution. Note that the reservoir flux and density are constants in Equations (17) and (18), respectively, while the wall contributions of both equations are a function of the wall location. And the origin of the coordinate system is the upstream center of the cylindrical aperture. Finally note that as shown in Figure 5, the flux determined in this study is in the axially downstream direction.

To solve Equations (17) and (18), the variables α_{o-c}, δ_{o-c}, L_{o-c}, α_{w-c}, δ_{w-c}, and L_{w-c} and must be defined as functions of R, t, r_o, r_w, φ, r, and z. For the reservoir's contribution, it can be shown that:

$$L_{o-c} = \sqrt{z^2 + r^2 + r_o^2 - 2 \cdot r \cdot r_o \cdot \cos(\varphi)} \tag{19}$$

and:

$$\alpha_{o-c} = \delta_{c-o} = \arccos\left\{ \frac{z}{L_{o-c}} \right\} \tag{20}$$

For the aperture wall's contribution, it can be shown that:

$$L_{w-c} = \sqrt{(z - z_w)^2 + r^2 + R^2 - 2 \cdot r \cdot R \cdot \cos(\varphi)} \tag{21}$$

$$\alpha_{w-c} = \arccos\left\{ \frac{R - r \cdot \cos(\varphi)}{L_{w-c}} \right\} \tag{22}$$

and:

$$\delta_{c-w} = \arccos\left\{ \frac{z - z_w}{L_{w-c}} \right\} \tag{23}$$

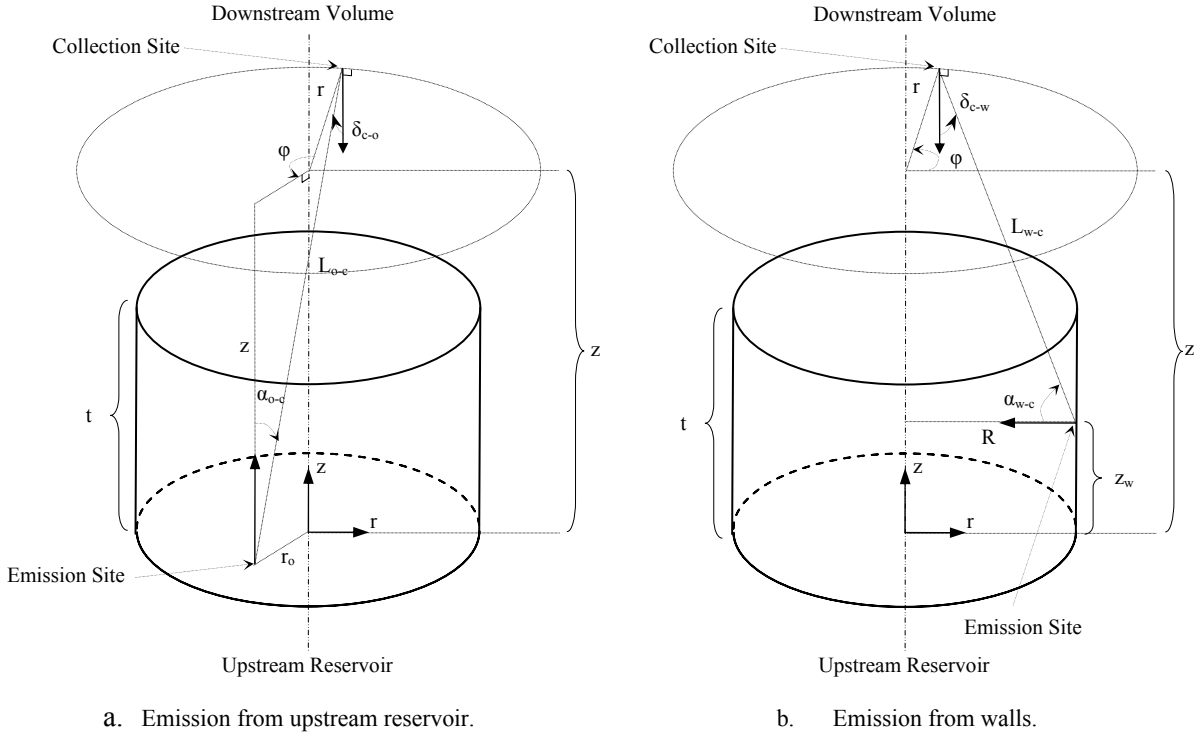a. Emission from upstream reservoir. b. Emission from walls.

Figure 5.—Sketch of the aperture geometry for determining particle fluxes and densities from an upstream reservoir and wall to a collection surface. Although the collection site is shown to be in the downstream region, the resulting equations will be applicable to all regions.

Equations (19) to (23) can be substituted into Equations (17) and (18) to yield the equations for the flux and density surrounding a cylindrical aperture. Note that there is symmetry about φ, so numerical integration can be simplified by integrating only half of the φ integral and multiplying the result by 2. The resulting flux is given in non-dimensional form by:

$$\overline{\Gamma}(\overline{r},\overline{z}) = \frac{2}{\pi}\cdot\left\{\int_{\varphi_{o,i}}^{\varphi_{o,f}}\int_{\overline{r}_{o,i}}^{\overline{r}_{o,f}}\frac{\overline{z}^2\cdot\overline{r}_o}{\left[\overline{z}^2+\overline{r}^2+\overline{r}_o^2-2\cdot\overline{r}\cdot\overline{r}_o\cdot\cos(\varphi)\right]^2}\cdot d\overline{r}_o\cdot d\varphi + \int_{\varphi_{w,i}}^{\varphi_{w,f}}\int_{\overline{z}_{w,i}}^{\overline{z}_{w,f}}\frac{\overline{\Gamma}_w(\overline{z}_w)\cdot(\overline{z}-\overline{z}_w)\cdot(1-\overline{r}\cdot\cos(\varphi))}{\left[(\overline{z}-\overline{z}_w)^2+\overline{r}^2+1-2\cdot\overline{r}\cdot\cos(\varphi)\right]^2}\cdot d\overline{z}_w\cdot d\varphi\right\} \qquad (24)$$

while the particle density is given by:

$$\overline{n}(\overline{r},\overline{z}) = \frac{1}{2\cdot\pi}\cdot\left\{\int_{\varphi_{o,i}}^{\varphi_{o,f}}\int_{\overline{r}_{o,i}}^{\overline{r}_{o,f}}\frac{\overline{z}\cdot\overline{r}_o}{\left[\overline{z}^2+\overline{r}^2+\overline{r}_o^2-2\cdot\overline{r}\cdot\overline{r}_o\cdot\cos(\varphi)\right]^{\frac{3}{2}}}\cdot d\overline{r}_o\cdot d\varphi + \int_{\varphi_{w,i}}^{\varphi_{w,f}}\int_{\overline{z}_{w,i}}^{\overline{z}_{w,f}}\frac{\overline{\Gamma}_w(\overline{z}_w)\cdot(1-\overline{r}\cdot\cos(\varphi))}{\left[(\overline{z}-\overline{z}_w)^2+\overline{r}^2+1-2\cdot\overline{r}\cdot\cos(\varphi)\right]^{\frac{3}{2}}}\cdot d\overline{z}_w\cdot d\varphi\right\} \qquad (25)$$

For both equations above, all dimensions (r, z, t, r_o, and z_w) are non-dimensionalized with the aperture radius, R, all fluxes are non-dimensionalized with the reservoir flux, Γ_o, and all densities are non-dimensionalized with the reservoir density, n_o. The "i" and "f" subscripts for the limits of integration denote initial and final locations. It is possible to integrate with respect to r_o and z_w (i.e., the inner integral of each double integral) in the equations above after substituting Equation (14) into Equations (24) and (25). So, the equation for particle flux can be rewritten as:

$$\overline{\Gamma}(\overline{r},\overline{z}) = \overline{\Gamma}_o(\overline{r},\overline{z}) + \overline{\Gamma}_w(\overline{r},\overline{z}) \qquad (26)$$

where the reservoir's contribution is given by:

$$\overline{\Gamma}_o\left(\overline{r},\overline{z}\right)=\frac{\overline{z}^2}{\pi}\cdot\int\limits_{\varphi_{o,i}}^{\varphi_{o,f}}\left\{\frac{\overline{r}\cdot\overline{r}_o\cdot\cos(\varphi)-\overline{z}^2-\overline{r}^2}{\left[\overline{r}^2\cdot\sin(\varphi)^2+\overline{z}^2\right]\cdot\left[\overline{z}^2+\overline{r}^2+\overline{r}_o^2-2\cdot\overline{r}\cdot\overline{r}_o\cdot\cos(\varphi)\right]}+\frac{\overline{r}\cdot\cos(\varphi)}{\left[\overline{r}^2\cdot\sin(\varphi)^2+\overline{z}^2\right]^{\frac{3}{2}}}\cdot\arctan\left[\frac{\overline{r}_o-\overline{r}\cdot\cos(\varphi)}{\sqrt{\overline{r}^2\cdot\sin(\varphi)^2+\overline{z}^2}}\right]\right\}\Bigg|_{\overline{r}_{o,i}}^{\overline{r}_{o,f}}\cdot d\varphi \quad (27)$$

and the wall's contribution is given by:

$$\overline{\Gamma}_w\left(\overline{r},\overline{z}\right)=\frac{1}{\pi}\cdot\int\limits_{\varphi_{w,i}}^{\varphi_{w,f}}\left\{\left[1-\overline{r}\cdot\cos(\varphi)\right]\cdot\left(\frac{a+b\cdot\overline{z}_w}{\left(\overline{z}-\overline{z}_w\right)^2+\overline{r}^2+1-2\cdot\overline{r}\cdot\cos(\varphi)}+\frac{b}{\sqrt{\overline{r}^2+1-2\cdot\overline{r}\cdot\cos(\varphi)}}\cdot\arctan\left[\frac{\overline{z}-\overline{z}_w}{\sqrt{\overline{r}^2+1-2\cdot\overline{r}\cdot\cos(\varphi)}}\right]\right)\right\}\Bigg|_{\overline{z}_{w,i}}^{\overline{z}_{w,f}}\cdot d\varphi \quad (28)$$

Likewise, the equation for the particle density is given by:

$$\overline{n}\left(\overline{r},\overline{z}\right)=\overline{n}_o\left(\overline{r},\overline{z}\right)+\overline{n}_w\left(\overline{r},\overline{z}\right) \quad (29)$$

where the reservoir's contribution is given by:

$$\overline{n}_o\left(\overline{r},\overline{z}\right)=\frac{\overline{z}}{2\cdot\pi}\cdot\int\limits_{\varphi_{o,i}}^{\varphi_{o,f}}\left\{\frac{\left[\overline{r}\cdot\overline{r}_o\cdot\cos(\varphi)-\overline{z}^2-\overline{r}^2\right]}{\left[\overline{z}^2+\overline{r}^2\cdot\sin(\varphi)^2\right]\cdot\sqrt{\overline{z}^2+\overline{r}^2+\overline{r}_o^2-2\cdot\overline{r}\cdot\overline{r}_o\cdot\cos(\phi)}}\right\}\Bigg|_{\overline{r}_{o,i}}^{\overline{r}_{o,f}}\cdot d\varphi \quad (30)$$

and the wall's contribution is given by:

$$\overline{n}_w\left(\overline{r},\overline{z}\right)=\frac{1}{2\cdot\pi}\cdot\int\limits_{\varphi_{w,i}}^{\varphi_{w,f}}\left\{\frac{\left(\overline{r}\cdot\cos(\varphi)-1\right)\cdot\left[\left(a+b\cdot\overline{z}\right)\cdot\left(\overline{z}-\overline{z}_w\right)+b\cdot\left(\overline{r}^2+1-2\cdot\overline{r}\cdot\cos(\varphi)\right)\right]}{\left[\overline{r}^2+1-2\cdot\overline{r}\cdot\cos(\varphi)\right]\cdot\sqrt{\left(\overline{z}-\overline{z}_w\right)^2+\overline{r}^2+1-2\cdot\overline{r}\cdot\cos(\varphi)}}\right\}\Bigg|_{\overline{z}_{w,i}}^{\overline{z}_{w,f}}\cdot d\varphi \quad (31)$$

B. Development of Limits of Integration for the Flux and Density Base Equations

With the base equations for particle flux and density developed, all that remains is defining the limits of integration. However, the limits of integration are not necessarily constant but can be variable (i.e., functions of r, z, and the aperture geometry). As shown in the prior section, the particle flux and density at any location surrounding a cylindrical aperture is made up of particles that have a direct line-of-sight from the reservoir and the aperture walls. The limits of integration are, therefore, a function of this desired location (i.e., r and z) as well as the aperture geometry. Specifically, the contribution of the reservoir and walls depends on which portion of each area has a direct line-of-sight to the location of interest. This is illustrated in Figures 6 and 7. As shown in the figures, all reservoir and cylindrical wall areas have a direct line-of-sight to downstream locations within region I. But only a portion of the reservoir and cylindrical wall areas have a direct line-of-sight to downstream locations within regions II and III. And no reservoir particles have a direct-line of sight to downstream locations in region IV.

In addition to this, there are three volumes surrounding a cylindrical aperture where the particle flux and density are desired. These volumes include the downstream, aperture interior, and upstream volumes. The equations developed for the downstream volume will be applicable to the interior volume, but a separate set of equations will be required for the upstream volume.

Though complicated, the division of the space surrounding a cylindrical aperture into separate volumes and regions with different limits of integration illustrated in Figures 6 and 7 will used to develop a set of equations that can rigorously determine the particle flux and density surrounding a cylindrical aperture. The following sections will determine the borders between the different regions and their respective limits of integration.
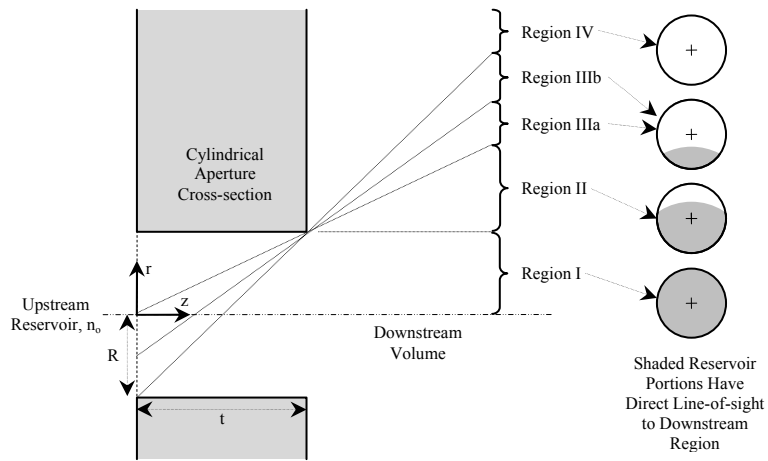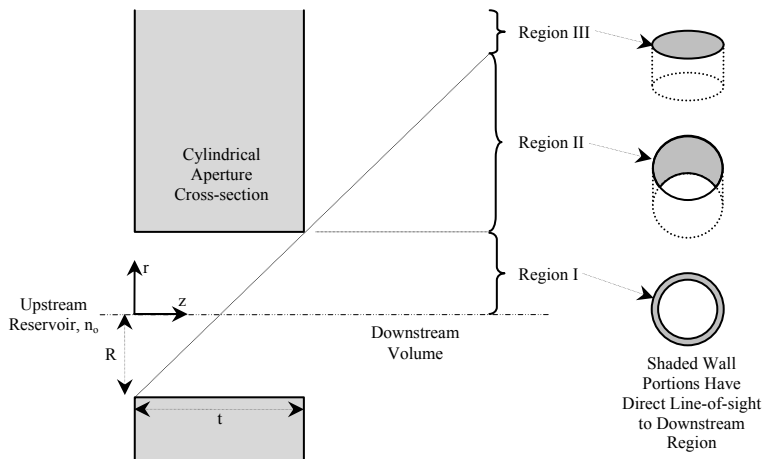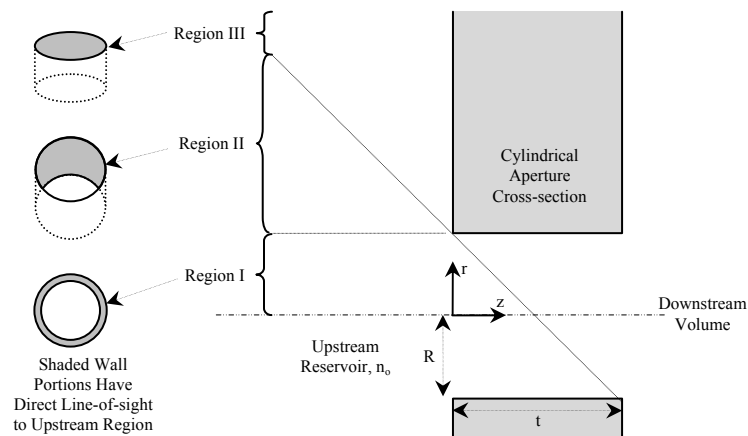
Figure 6.—Definition of downstream regions for the development of the variable limits of integration for the particle flux from an upstream reservoir.

a. Downstream and Interior Volumes

b. Upstream Volume

Figure 7.—Definition of regions for the development of the variable limits of integration for the particle flux from the aperture walls.

1. Reservoir Contribution: Interior Volume and Downstream Volume—Region I

As shown in Figure 6, there is a direct line of sight from any location to the entire reservoir surface as long as the following radial and axial border conditions are met:

$$\bar{r} \le 1 \ \text{ and } \ \bar{z} > 0 \tag{32}$$

As a result, the limits of integration for Equations (27) and (30) are constants (i.e., independent of r and z) and equal to 0 to π for φ and 0 to 1 for $\bar{r}_o$.

2. Reservoir Contribution: Downstream Volume—Region II

Figure 6 shows region II of the downstream volume. It can easily be shown that region II is defined by the following radial and axial border conditions:

$$1 < \bar{r} \le \frac{\bar{z}}{\bar{t}} \ \text{ and } \ \bar{z} > \bar{t} \tag{33}$$

Figure 8 shows the geometry of region II in greater detail. The shaded region in the figure has two different radii: r_{oII} when φ is between 0 and φ_{oII}; and R when φ is between φ_{oII} and π. As a result, integration for this case is slightly more complicated because the integrals of Equations (27) and (30) must be split into the summation of two integrals. For the first integral, it can be inferred from the figure that limits of integration along φ from 0 to φ_{oII} will be between 0 and r_{oII} for r_o. The second integral's limits of integration along φ between φ_{oII} and π will be from 0 to R for r_o.

The limits r_{oII} and φ_{oII} must be defined as functions of r and z. The limit r_{oII} is also a function of φ, which can be inferred from Figure 8, so the double integrals of Equations (27) and (30) must be integrated with respect to r_o first. The limit r_{oII} is determined by noting that triangles at axial locations t and z in Figure 8 share a common angle, γ. The law of cosines is applied to the angle φ for the triangle at z to determine $\tan(\alpha)$. The law of cosines is applied again to both triangles for the angle γ and the $\cos(\gamma)$ terms of each equation are equated to determine r_{oII}. It can be shown that r_{oII} is given in non-dimensional for by:

$$\bar{r}_{oII}(\bar{r}, \bar{z}, \varphi) = \frac{-\dfrac{\bar{t} \cdot \bar{r}}{\bar{z}} \cdot \cos(\varphi) + \sqrt{1 - \left(\dfrac{\bar{t} \cdot \bar{r}}{\bar{z}}\right)^2 \cdot \sin(\varphi)^2}}{1 - \dfrac{\bar{t}}{\bar{z}}} \tag{34}$$
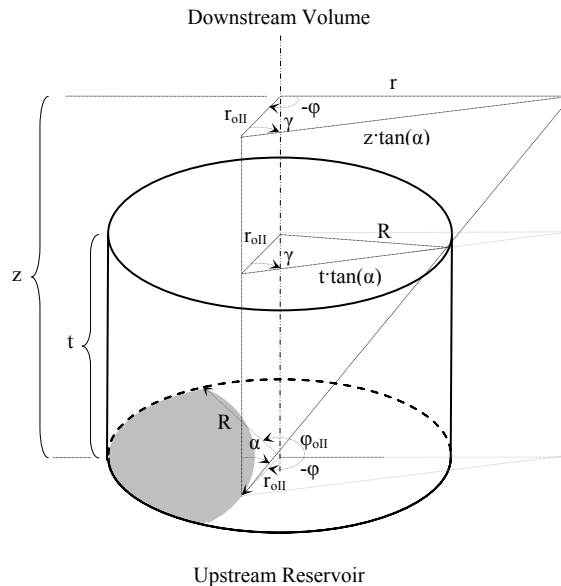

Figure 8.—Development of the reservoir's contribution to region II of the downstream volume. The shaded reservoir region contributes to the downstream flux and density.

To solve for φ_{oII}, the equation above is set equal to R (or 1 in non-dimensional form) and solved for φ. The result in non-dimensional form is given by:

$$\varphi_{oII}(\bar{r}, \bar{z}) = \arccos\left[\frac{1 - \left(1 - \dfrac{\bar{t}}{\bar{z}}\right)^2 - \left(\dfrac{\bar{t} \cdot \bar{r}}{\bar{z}}\right)^2}{2 \cdot \dfrac{\bar{t} \cdot \bar{r}}{\bar{z}} \cdot \left(1 - \dfrac{\bar{t}}{\bar{z}}\right)}\right] \tag{35}$$

3. Reservoir Contribution: Downstream Volume—Region III

Figure 6 shows regions IIIa and IIIb of the downstream volume. Region III is similar to region II, with the only difference being that shaded region in Figure 9 does not include the center of the aperture as it does in Figure 8 for region II. In fact, the equations for r_{oII} and φ_{oII} are still applicable in region III. However, the geometry of this region is more complicated, requiring that it be further divided into two separate regions (i.e., IIIa and IIIb). The reason for this can be better understood by examining Figure 10, which shows the reservoir's contribution at the aperture entrance. In this figure, the projected area is the circular area formed when viewing upstream from a downstream location through the aperture exit plane. It can be shown that the radius of this projected area, R_p, is R/(1-t/z). The variable φ_{omax} is the angle along φ where the radii of the aperture entrance and the projected area circles intersect to form a 90° angle, as shown in Figure 10. It can be shown that:

$$\phi_{o\max}(\bar{r}, \bar{z}) = \pi - \arcsin\left(\frac{\bar{z}}{\bar{t} \cdot \bar{r}}\right) \tag{36}$$

Figure 9.—Development of the reservoir's contribution to region III of the downstream volume. The shaded reservoir region contributes to the downstream flux and density.

a. Region IIIa   b. Region IIIb
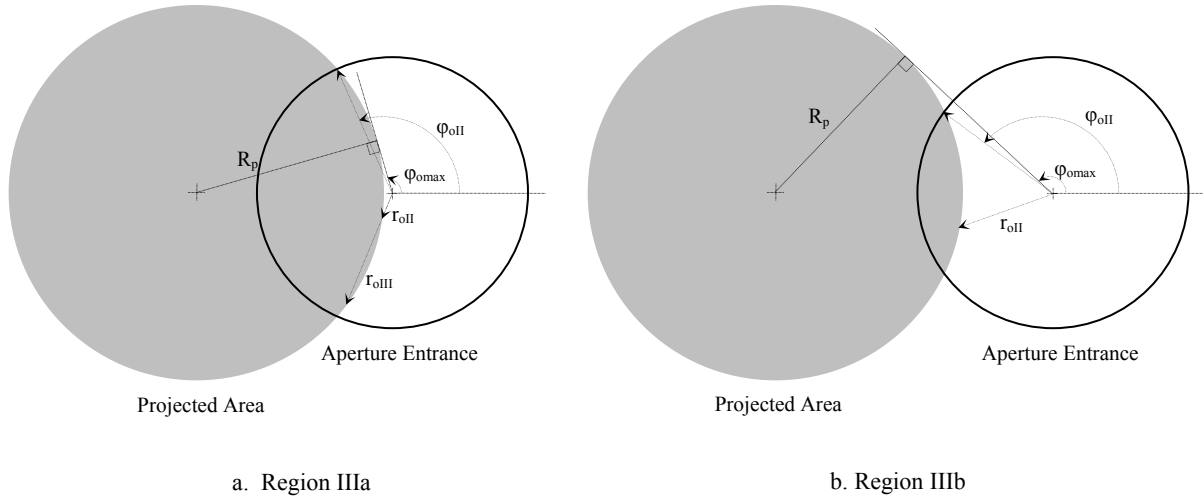
Figure 10.—Top view of the reservoir's contribution to region III of the downstream volume.

In region IIIa, the point of intersection for the radial lines used to define φ_{omax} lies within the radius of the aperture, R. This creates some complexity for determining the limits of integration for Equations (27) and (30). For $\varphi < \varphi_{oII}$ in region IIIa, it can be shown that the distance r_o to the edge of the shaded region is r_{oII} as given in Equation (34). So, the limits of integration are from r_{oII} to R between φ_{oII} and π. However, between φ_{omax} and φ_{oII}, integration occurs between r_{oII} and r_{oIII}, as shown in Figure 10. Using Figure 9 and the same process as that used to determine Equation (34), it can be shown that r_{oIII} is given in non-dimensional form by:

$$\bar{r}_{oIII}(\bar{r}, \bar{z}, \varphi) = \frac{-\dfrac{\bar{t} \cdot \bar{r}}{\bar{z}} \cdot \cos(\phi) - \sqrt{1 - \left(\dfrac{\bar{t} \cdot \bar{r}}{\bar{z}}\right)^2 \cdot \sin(\phi)^2}}{1 - \dfrac{\bar{t}}{\bar{z}}} \tag{37}$$

In region IIIb the point of intersection for the radial lines used to define φ_{omax} lies outside the aperture entrance. This simplifies the the limits of integration for Equations (27) and (30). As shown in Figure 10, the distance r_o to the edge of the shaded region is still r_{oII} of Equation (34). And the limits of integration are from r_{oII} to R between φ_{oII} and π.

The border between regions IIIa and IIIb is determined by placing the point of intersection for the radial lines used to define φ_{omax} at the aperture radius, R, and solving for the downstream radius as a function of axial location. So, region IIIa is defined by the following radial and axial border conditions:

$$\frac{\bar{z}}{\bar{t}} < \bar{r} \leq \left[\frac{\bar{z}}{\bar{t}} \cdot \sqrt{\left(1 - \frac{\bar{t}}{\bar{z}}\right)^2} + 1 \right] \text{ and } \bar{z} > \bar{t} \tag{38}$$

Defining the border conditions for region IIIb requires defining the border between regions IIIb and IV. For Figure 6, it can easily be shown that this border is given by $r = (2 \cdot z/t - R)$. So, region IIIb is defined by the following radial and axial border conditions:

$$\left[\frac{\bar{z}}{\bar{t}} \cdot \sqrt{\left(1 - \frac{\bar{t}}{\bar{z}}\right)^2} + 1 \right] < \bar{r} \leq \left(2 \cdot \frac{\bar{z}}{\bar{t}} - 1 \right) \text{ and } \bar{z} > \bar{t} \tag{39}$$

4. Reservoir Contribution: Downstream Volume—Regions IV

As shown in Figure 6, there is no direct line of sight from the reservoir to region IV of the downstream volume. As a result, the particle flux and density contributions from the reservoir will be 0 for this region, which is defined by the following radial and axial border conditions:

$$\bar{r} > \left(2 \cdot \frac{\bar{z}}{\bar{t}} - 1 \right) \text{ and } \bar{z} > \bar{t} \tag{40}$$

5. Reservoir Contribution: Upstream Volume

Narasimha solved for the particle flux and density surrounding a thin circular aperture (i.e., so thin that the thickness can be neglected) (Ref. 13). He found that there was symmetry about the aperture such that the upstream density could be determined with downstream density. For a spherical coordinate system, the reservoir particle density is given in non-dimensional form by:

$$\bar{n}_{o,up} (r, \pi - \theta) = 1 - \bar{n}_o (r, \theta) \tag{41}$$

where $n_{o,up}$ is the reservoir's contribution to the upstream particle density. Transforming coordinate systems from spherical to cylindrical, it can be shown that the reservoir's contribution to the upstream particle density is given in non-dimensional form by:

$$\bar{n}_{o,up} (\bar{r}, \bar{z}) = 1 - \bar{n}_o (\bar{r}, |\bar{z}|) \tag{42}$$

Here, n_o is given by Equation (30). By analogy, the reservoir's contribution to the upstream particle flux is given in non-dimensional form by:

$$\bar{\Gamma}_{o,up} (\bar{r}, \bar{z}) = \bar{\Gamma}_o (\bar{r}, |\bar{z}|) \tag{43}$$

Here, Γ_o is given by Equation (27). Later, it will be shown that Equations (27) and (30) decrease as z and r increase in magnitude. So at locations far upstream of the aperture, Equation (42) approaches n_o (or unity in non-dimensional form), as would be expected because this is the reservoir's density. However, Equation (43) approaches zero at these locations because the net axial flux should be zero at these locations due to the isotropic velocity assumption.

6. Wall Contribution: Upstream, Interior, and Downstream Volumes—Region I

As shown in Figure 7, there is a direct line of sight from any location to the entire aperture wall surface as long as the following radial border condition is met:

$$\bar{r} \le 1 \tag{44}$$

This is true for any volume (upstream, interior, or downstream), so there is no axial border condition. As a result, the limits of integration for Equations (28) and (31) are constants (i.e., independent of r and z) and equal to 0 to π for φ and 0 to $\bar{t}$ for $\bar{z}_w$.

7. Wall Contribution: Downstream Volume—Region II

Figure 7 shows region II of the downstream volume. It can easily be shown that region II is defined by the following radial and axial border conditions:

$$1 < \bar{r} \le \left(2 \cdot \frac{\bar{z}}{\bar{t}} - 1 \right) \text{ and } \bar{z} > \bar{t} \tag{45}$$
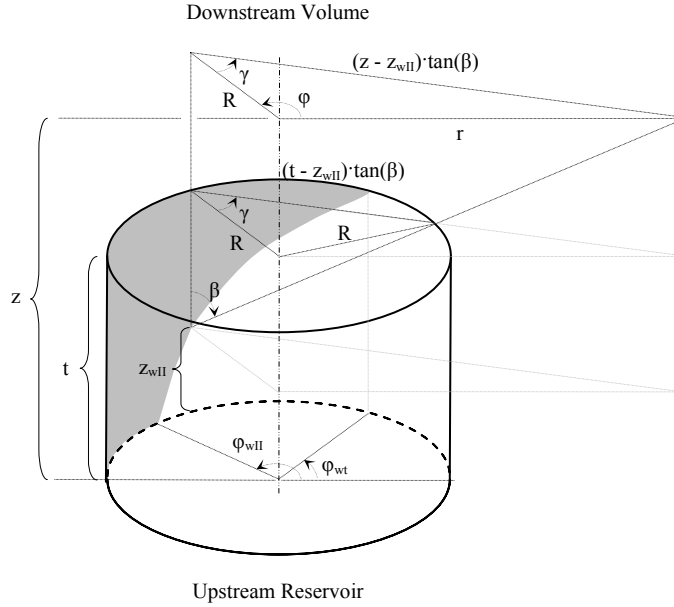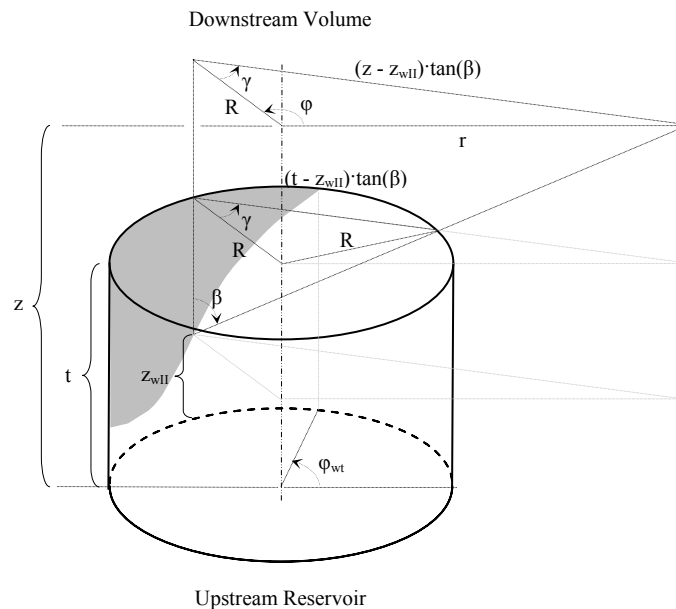
Figure 11.—Development of the aperture wall's contribution to region II of the downstream volume. Only the shaded wall surface contributes to the downstream flux and density. Only half of the shaded region is shown.

Figure 11 shows the geometry of region II in greater detail. Integration for this case is slightly more complicated in that the integrals of Equations (28) and (31) have to be split into the summation of two integrals. It can be inferred from the figure that the first integral's limits of integration will be between φ_{wt} and φ_{wII}, for z_w from z_{wII} to t. The second integral's limits of integration will be between φ_{wII} and π for z_w from 0 to t.

The limits z_{wII}, φ_{wII}, and φ_{wt} must be defined as functions of r and z. The limit z_{wII} is also a function of φ, which can be inferred from Figure 11, so the double integrals of Equations (28) and (31) must be integrated with respect to z_w first. The limit z_{wII} is determined as was done for the reservoir. Note that the triangles at $z = t$ and z in Figure 11 share a common angle, γ. The law of cosines is applied to the angle φ for the triangle at z to determine $\tan(\beta)$. The law of cosines is applied again to both triangles at t and z for the angle γ and the $\cos(\gamma)$ terms of each equation are equated to determine z_{wII}. It can be shown that z_{wII} is given in non-dimensional for by:

$$\bar{z}_{wII}(\bar{r}, \bar{z}, \varphi) = \frac{\bar{r}^2 \cdot \bar{t} + \bar{t} - 2 \cdot \bar{z} - 2 \cdot \bar{r} \cdot (\bar{t} - \bar{z}) \cdot \cos(\varphi)}{\bar{r}^2 - 1} \tag{46}$$

To solve for φ_{wII}, the equation above is set equal to 0 and solved for φ. The result in non-dimensional form is given by:

$$\varphi_{wII}(\bar{r}, \bar{z}) = \arccos\left[\frac{\bar{r}^2 + 1 - 2 \cdot \dfrac{\bar{z}}{\bar{t}}}{2 \cdot \bar{r} \cdot \left(1 - \dfrac{\bar{z}}{\bar{t}}\right)}\right] \tag{47}$$

To solve for φ_{wt}, the equation for z_{wII} above is set equal to t and solved for φ. The result in non-dimensional form is given by:

$$\varphi_{wt}(\bar{r}, \bar{z}) = \arccos\left(\frac{1}{\bar{r}}\right) \tag{48}$$

8. Wall Contribution: Downstream Volume—Region III

Figure 7 shows region III of the downstream volume. It can easily be shown that region III is defined by the following radial and axial border conditions:

$$\bar{r} > \left(2 \cdot \frac{\bar{z}}{\bar{t}} - 1 \right) \text{ and } \bar{z} > \bar{t} \tag{49}$$

Figure 12 shows the geometry of region III in greater detail. Integration of Equations (28) and (31) for this case is less complicated than region II. It can be inferred from the figure that the integral's limits of integration will be between φ_{wt} and π for z_w from z_{wII} to t. Note in Figure 12 that the equations for φ_{wt} and z_{wII} are the same as those for region II.

9. Wall Contribution: Upstream Volume—Region II

Figure 7 shows region II of the upstream reservoir. It can easily be shown that region II is defined by the following radial and axial border conditions:

$$1 < \bar{r} \leq \left(1 - 2 \cdot \frac{\bar{z}}{\bar{t}} \right) \text{ and } \bar{z} < 0 \tag{50}$$

Figure 13 shows the geometry of region II in greater detail. As with the downstream case, integration for this case is slightly more complicated because the integrals of Equations (28) and (31) have to be split into the summation of two integrals. It can be inferred from the figure that the first integral's limits of integration will be between φ_{wt} and φ_{wIIn}, where integration along z_w will be between 0 and z_{wIIn}. The second integral's limits of integration will be between φ_{wIIn} and π, where integration along z_w will be between 0 and t.
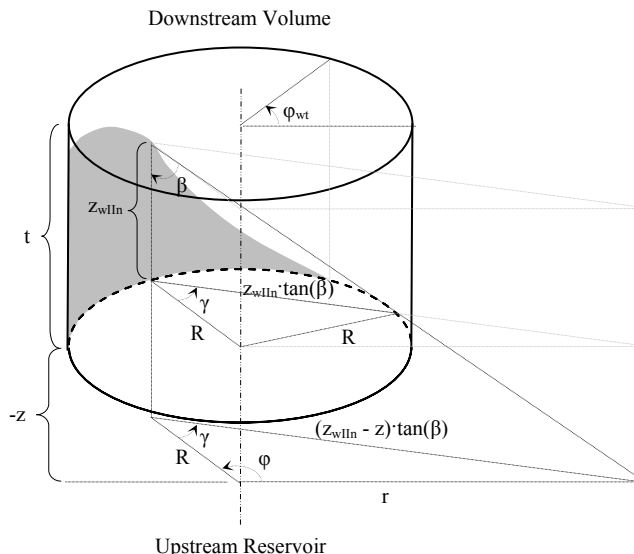

Figure 12.—Development of the aperture wall's contribution to region III of the downstream volume. Only the shaded wall surface contributes to the downstream flux and density. Only half of the shaded region is shown.
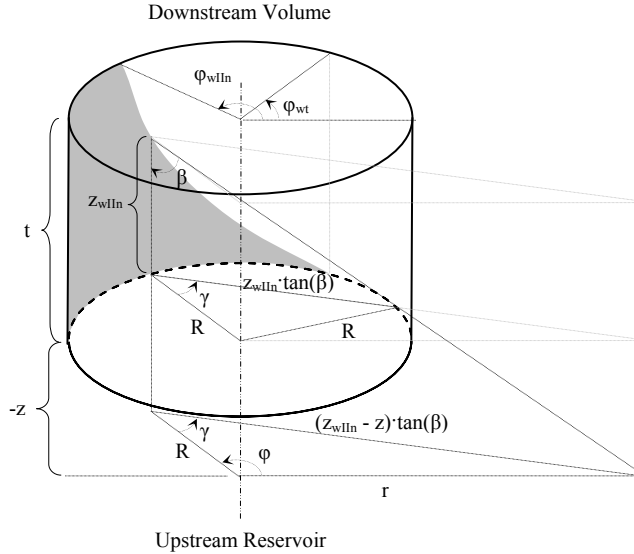
Figure 13.—Development of the aperture wall's contribution to region II of the upstream volume. Only the shaded wall surface contributes to the downstream flux and density. Only half of the shaded region is shown.

The limits z_{wIIn}, φ_{wIIn}, and φ_{wt} must be defined as functions of r and z. The limit z_{wIIn} is also a function of φ, which can be inferred from Figure 13, so the double integrals of Equations (28) and (31) must be integrated with respect to z_w first. The limit z_{wIIn} is determined as was done for the reservoir. Note that the triangles at $z = 0$ and $-z$ in Figure 13 share a common angle, γ. The law of cosines is applied to the angle φ for the triangle at z to determine $\tan(\beta)$. The law of cosines is applied again to both triangles at t and z for the angle γ and the $\cos(\gamma)$ terms of each equation are equated to determine z_{wIIn}. It can be shown that z_{wIIn} is given in non-dimensional for by:

$$\overline{z}_{wIIn}(\overline{r}, \overline{z}, \varphi) = 2 \cdot \overline{z} \cdot \frac{1 - \overline{r} \cdot \cos(\varphi)}{1 - \overline{r}^2} \tag{51}$$

To solve for φ_{wIIn}, the equation above is set equal to t and solved for φ. The result in non-dimensional form is given by:

$$\varphi_{wIIn}(\overline{r}, \overline{z}) = \arccos\left[\frac{\overline{r}^2 - 1 + 2 \cdot \dfrac{\overline{z}}{\overline{t}}}{2 \cdot \overline{r} \cdot \dfrac{\overline{z}}{\overline{t}}}\right] \tag{52}$$

The equation for φ_{wt} is given in Equation (48).

10. Wall Contribution: Upstream Volume—Region III

Figure 7 shows region III of the upstream volume. It can easily be shown that region III is defined by the following radial and axial border conditions:

$$\overline{r} > \left(1 - 2 \cdot \frac{\overline{z}}{\overline{t}}\right) \text{ and } \overline{z} < 0 \tag{53}$$

Figure 14 shows the geometry of region III in greater detail. Integration of Equations (28) and (31) for this case is less complicated than region II. It can be inferred from the figure that the integral's limits of integration will be between φ_{wt} and π, where integration along z_w will be between 0 and z_{wII}. Note in Figure 14 that the equations for φ_{wt} and z_{wIIn} are the same as those for region II.

Downstream Volume

Figure 14.—Development of the aperture wall's contribution
to region III of the upstream volume. Only the shaded wall
surface contributes to the downstream flux and density.
Only half of the shaded region is shown.

C. Equations for Flux and Particle Density Surrounding a Cylindrical Aperture

The limits of integration defined in the previous section can be substituted into Equations (27) and (28) for particle flux and Equations (30) and (31) for particle density. Because the surrounding aperture had to be divided into separate volumes and regions as illustrated in Figures 6 and 7, the radial and axial border conditions defined in the previous sections are used to determine the appropriate particle flux or density equation. The results are listed in Tables 1 to 5. The particle flux in the axial direction is given by Equation (26), with the reservoir's contribution equations listed in Table 1 and the wall's contribution equations listed in Table 2. The particle density is given by Equation (29), with the reservoir's contribution equations listed in Table 3 and the wall's contribution equations listed in Table 4. Table 5 lists the variable limits of integration equations used in Tables 1 to 4.

The integrals remaining in Equations (27), (28), (30), and (31) could only be solved in two cases, which included the flux equations for region I of the downstream and interior volumes and for the upstream volume (see Table 1). The remaining integrals in Tables 1 to 4 must be solved numerically.

It can be shown that the particle density equation for the reservoir's contribution in region I produces a singularity at $r = z = 0$. This is easily overcome by noting that the reservoir's contribution to particle density is 1/2 at the aperture entrance (i.e., $z = 0$), and is independent of radial location (Ref. 11).

The particle transmission probability, P, through the cylindrical aperture (i.e., the fraction of particles incident upon the aperture inlet that eventually pass through) can also be determined (Ref. 7). The probability is given by integrating the total particle flux radially at any axial location and dividing by the particle flux at the aperture inlet:

$$P(\bar{z}) = \frac{\int\limits_{0}^{2\cdot\pi}\int\limits_{0}^{\infty}\Gamma(r,z)\cdot r \cdot dr \cdot d\varphi}{\Gamma_{o} \cdot \int\limits_{0}^{2\cdot\pi}\int\limits_{0}^{R} r \cdot dr \cdot d\varphi} = 2 \cdot \int\limits_{0}^{\infty}\overline{\Gamma}(\bar{r},\bar{z})\cdot \bar{r} \cdot d\bar{r} \tag{54}$$

Within the cylindrical aperture (i.e., $0 \leq z \leq t$), the upper limit of integration along r changes from ∞ to R (or 1 in non-dimensional form). Because the transmission probability can be calculated at any axial location and still yield the same result, this equation also serves as a useful tool to verify the equations in Tables 1, 2, and 5. And because particle density equations utilize the same equations except for the $\cos(\delta)$ terms, it can indirectly verify the equations in Tables 3 and 4.

TABLE 1.—EQUATIONS FOR THE RESERVOIR'S CONTRIBUTION TO THE PARTICLE FLUX IN THE AXIAL DIRECTION FOR THE DIFFERENT REGIONS OF FIGURE 6

Region	Equation	Border conditionals
	Downstream and Interior volumes	
I	$\bar{\Gamma}_o(\bar{r},\bar{z}) = \dfrac{1}{2}\cdot\left[1 - \dfrac{\bar{z}^2+\bar{r}^2-1}{\sqrt{(\bar{z}^2+\bar{r}^2+1)^2-4\cdot\bar{r}^2}}\right]$	$\bar{r}\le 1$
II	$\begin{aligned}\bar{\Gamma}_o(\bar{r},\bar{z}) = {}&\dfrac{\bar{z}^2}{\pi}\cdot\int_0^{\varphi_{oII}(\bar{r},\bar{z})}\Bigg[\dfrac{\bar{r}\cdot\bar{r}_{oII}(\bar{r},\bar{z},\varphi)\cdot\cos(\varphi)-\bar{z}^2-\bar{r}^2}{\left[\bar{r}^2\cdot\sin(\varphi)^2+\bar{z}^2\right]\cdot\left[\bar{r}_{oII}(\bar{r},\bar{z},\varphi)^2-2\cdot\bar{r}_{oII}(\bar{r},\bar{z},\varphi)\cdot\bar{r}\cdot\cos(\varphi)+\bar{z}^2+\bar{r}^2\right]}+\dfrac{-\bar{z}^2-\bar{r}^2}{\left[\bar{r}^2\cdot\sin(\varphi)^2+\bar{z}^2\right]\cdot(\bar{z}^2+\bar{r}^2)}-\dfrac{\bar{r}\cdot\cos(\varphi)}{\left[\bar{r}^2\cdot\sin(\varphi)^2+\bar{z}^2\right]^{\frac{3}{2}}}\cdot\arctan\left[\dfrac{-\bar{r}\cdot\cos(\varphi)}{\sqrt{\bar{r}^2\cdot\sin(\varphi)^2+\bar{z}^2}}\right]+\dfrac{\bar{r}\cdot\cos(\varphi)}{\left[\bar{r}^2\cdot\sin(\varphi)^2+\bar{z}^2\right]^{\frac{3}{2}}}\cdot\arctan\left[\dfrac{\bar{r}_{oII}(\bar{r},\bar{z},\varphi)-\bar{r}\cdot\cos(\varphi)}{\sqrt{\bar{r}^2\cdot\sin(\varphi)^2+\bar{z}^2}}\right]\Bigg]\cdot d\varphi\\[2mm]+{}&\dfrac{\bar{z}^2}{\pi}\cdot\int_{\varphi_{oII}(\bar{r},\bar{z})}^{\pi}\Bigg[\dfrac{\bar{r}\cdot\cos(\varphi)-\bar{z}^2-\bar{r}^2}{\left[\bar{r}^2\cdot\sin(\varphi)^2+\bar{z}^2\right]\cdot\left(1-2\cdot\bar{r}\cdot\cos(\varphi)+\bar{z}^2+\bar{r}^2\right)}+\dfrac{-\bar{z}^2-\bar{r}^2}{\left[\bar{r}^2\cdot\sin(\varphi)^2+\bar{z}^2\right]\cdot(\bar{z}^2+\bar{r}^2)}-\dfrac{\bar{r}\cdot\cos(\varphi)}{\left[\bar{r}^2\cdot\sin(\varphi)^2+\bar{z}^2\right]^{\frac{3}{2}}}\cdot\arctan\left[\dfrac{-\bar{r}\cdot\cos(\varphi)}{\sqrt{\bar{r}^2\cdot\sin(\varphi)^2+\bar{z}^2}}\right]+\dfrac{\bar{r}\cdot\cos(\varphi)}{\left[\bar{r}^2\cdot\sin(\varphi)^2+\bar{z}^2\right]^{\frac{3}{2}}}\cdot\arctan\left[\dfrac{1-\bar{r}\cdot\cos(\varphi)}{\sqrt{\bar{r}^2\cdot\sin(\varphi)^2+\bar{z}^2}}\right]\Bigg]\cdot d\varphi\end{aligned}$	$1<\bar{r}\le\dfrac{\bar{z}}{t}$ and $\bar{z}>t$
IIIa	$\begin{aligned}\bar{\Gamma}_o(\bar{r},\bar{z}) = {}&\dfrac{\bar{z}^2}{\pi}\cdot\int_{\varphi_{oII}(\bar{r},\bar{z})}^{\varphi_{o\,max}(\bar{r},\bar{z})}\Bigg[\dfrac{\bar{r}\cdot\bar{r}_{oII}(\bar{r},\bar{z},\varphi)\cdot\cos(\varphi)-\bar{z}^2-\bar{r}^2}{\left[\bar{r}^2\cdot\sin(\varphi)^2+\bar{z}^2\right]\cdot\left[\bar{r}_{oII}(\bar{r},\bar{z},\varphi)^2-2\cdot\bar{r}_{oII}(\bar{r},\bar{z},\varphi)\cdot\bar{r}\cdot\cos(\varphi)+\bar{z}^2+\bar{r}^2\right]}+\dfrac{\bar{r}\cdot\cos(\varphi)}{\left[\bar{r}^2\cdot\sin(\varphi)^2+\bar{z}^2\right]^{\frac{3}{2}}}\cdot\arctan\left[\dfrac{\bar{r}_{oII}(\bar{r},\bar{z},\varphi)-\bar{r}\cdot\cos(\varphi)}{\sqrt{\bar{r}^2\cdot\sin(\varphi)^2+\bar{z}^2}}\right]\Bigg]\cdot d\varphi\\[2mm]+{}&\dfrac{\bar{z}^2}{\pi}\cdot\int_{\varphi_{oII}(\bar{r},\bar{z})}^{\pi}\Bigg[\dfrac{\bar{r}\cdot\cos(\varphi)-\bar{z}^2-\bar{r}^2}{\left[\bar{r}^2\cdot\sin(\varphi)^2+\bar{z}^2\right]\cdot\left(1-2\cdot\bar{r}\cdot\cos(\varphi)+\bar{z}^2+\bar{r}^2\right)}+\dfrac{1-\bar{r}\cdot\cos(\varphi)}{\left[\bar{r}^2\cdot\sin(\varphi)^2+\bar{z}^2\right]^{\frac{3}{2}}}\cdot\arctan\left[\dfrac{\bar{r}_{oIII}(\bar{r},\bar{z},\varphi)-\bar{r}\cdot\cos(\varphi)}{\sqrt{\bar{r}^2\cdot\sin(\varphi)^2+\bar{z}^2}}\right]\Bigg]\cdot d\varphi\end{aligned}$	$\dfrac{\bar{z}}{t}<\bar{r}\le\left[\dfrac{\bar{z}}{t}\cdot\sqrt{\left(1-\dfrac{t}{\bar{z}}\right)^2}+1\right]$ and $\bar{z}>t$
IIIb	$\bar{\Gamma}_o(\bar{r},\bar{z}) = \dfrac{\bar{z}^2}{\pi}\cdot\int_{\varphi_{oII}(\bar{r},\bar{z})}^{\pi}\Bigg[\dfrac{\bar{r}\cdot\bar{r}_{oIII}(\bar{r},\bar{z},\varphi)\cdot\cos(\varphi)-\bar{z}^2-\bar{r}^2}{\left[\bar{r}^2\cdot\sin(\varphi)^2+\bar{z}^2\right]\cdot\left[\bar{r}_{oIII}(\bar{r},\bar{z},\varphi)^2-2\cdot\bar{r}_{oIII}(\bar{r},\bar{z},\varphi)\cdot\bar{r}\cdot\cos(\varphi)+\bar{z}^2+\bar{r}^2\right]}+\dfrac{1-\bar{r}\cdot\cos(\varphi)}{\left[\bar{r}^2\cdot\sin(\varphi)^2+\bar{z}^2\right]^{\frac{3}{2}}}\cdot\arctan\left[\dfrac{\bar{r}_{oIII}(\bar{r},\bar{z},\varphi)-\bar{r}\cdot\cos(\varphi)}{\sqrt{\bar{r}^2\cdot\sin(\varphi)^2+\bar{z}^2}}\right]\Bigg]\cdot d\varphi$	$\left[\dfrac{\bar{z}}{t}\cdot\sqrt{\left(1-\dfrac{t}{\bar{z}}\right)^2}+1\right]<\bar{r}\le\left(2\cdot\dfrac{\bar{z}}{t}-1\right)$ and $\bar{z}>t$
IV	$\bar{\Gamma}_o(\bar{r},\bar{z}) = 0$	$\bar{r}>\left(2\cdot\dfrac{\bar{z}}{t}-1\right)$ and $\bar{z}>t$
	Upstream volume	
-	$\bar{\Gamma}_o(\bar{r},\bar{z}) = 1 - \dfrac{1}{2}\cdot\left[1 - \dfrac{\bar{z}^2+\bar{r}^2-1}{\sqrt{(\bar{z}^2+\bar{r}^2+1)^2-4\cdot\bar{r}^2}}\right]$	$\bar{z}<0$

TABLE 2.—EQUATIONS FOR THE APERTURE WALL'S CONTRIBUTION TO THE PARTICLE FLUX IN THE AXIAL DIRECTION FOR THE DIFFERENT REGIONS OF FIGURE 7

Region	Equation	Border conditionals
I	$$\overline{\Gamma}_w(\overline{r},\overline{z}) = 2 \cdot \int_0^{\overline{t}} (a + b \cdot \overline{z}_w) \cdot \frac{(\overline{z}-\overline{z}_w) \cdot \left[(\overline{z}-\overline{z}_w)^2 - \overline{r}^2 + 1\right]}{\left(\left[(\overline{z}-\overline{z}_w)^2 + \overline{r}^2 + 1\right]^2 - 4\cdot \overline{r}^2\right)^{\frac{3}{2}}} \cdot d\overline{z}_w$$	$\overline{r} \le 1$

Downstream and Interior volumes

Region	Equation	Border conditionals
II	$$\overline{\Gamma}_w(\overline{r},\overline{z}) = \frac{1}{\pi} \cdot \int_{\varphi_{wt}(\overline{r},\overline{z})}^{\varphi_{wII}(\overline{r},\overline{z})} [1 - \overline{r}\cdot\cos(\varphi)] \cdot \left[\frac{a + b\cdot\overline{t}}{(\overline{z}-\overline{t})^2 + \overline{r}^2 + 1 - 2\cdot\overline{r}\cdot\cos(\varphi)} + \frac{b}{\sqrt{\overline{r}^2+1-2\cdot\overline{r}\cdot\cos(\varphi)}} \cdot \arctan\frac{\overline{z}-\overline{t}}{\sqrt{\overline{r}^2+1-2\cdot\overline{r}\cdot\cos(\varphi)}} - \frac{a + b\cdot\overline{z}_{wII}(\overline{r},\overline{z},\varphi)}{(\overline{z}-\overline{z}_{wII}(\overline{r},\overline{z},\varphi))^2 + \overline{r}^2 + 1 - 2\cdot\overline{r}\cdot\cos(\varphi)} - \frac{b}{\sqrt{\overline{r}^2+1-2\cdot\overline{r}\cdot\cos(\varphi)}} \cdot \arctan\frac{\overline{z}-\overline{z}_{wII}(\overline{r},\overline{z},\varphi)}{\sqrt{\overline{r}^2+1-2\cdot\overline{r}\cdot\cos(\varphi)}} \right] \cdot d\varphi$$ $$+ \frac{1}{\pi} \cdot \int_{\varphi_{wII}(\overline{r},\overline{z})}^{\pi} [1-\overline{r}\cdot\cos(\varphi)] \cdot \left[\frac{a + b\cdot\overline{t}}{(\overline{z}-\overline{t})^2 + \overline{r}^2 + 1 - 2\cdot\overline{r}\cdot\cos(\phi)} + \frac{b}{\sqrt{\overline{r}^2+1-2\cdot\overline{r}\cdot\cos(\phi)}} \cdot \arctan\frac{\overline{z}-\overline{t}}{\sqrt{\overline{r}^2+1-2\cdot\overline{r}\cdot\cos(\phi)}} - \frac{a}{\overline{z}^2+\overline{r}^2+1-2\cdot\overline{r}\cdot\cos(\varphi)} - \frac{b}{\sqrt{\overline{r}^2+1-2\cdot\overline{r}\cdot\cos(\varphi)}} \cdot \arctan\frac{\overline{z}}{\sqrt{\overline{r}^2+1-2\cdot\overline{r}\cdot\cos(\varphi)}} \right] \cdot d\varphi$$	$1 < \overline{r} \le \left(2\cdot\frac{\overline{z}}{\overline{t}} - 1\right)$ and $\overline{z} > \overline{t}$
III	$$\overline{\Gamma}_w(\overline{r},\overline{z}) = \frac{1}{\pi} \cdot \int_{\varphi_{wt}(\overline{r},\overline{z})}^{\pi} [1-\overline{r}\cdot\cos(\varphi)] \cdot \left[\frac{a+b\cdot\overline{t}}{(\overline{z}-\overline{t})^2+\overline{r}^2+1-2\cdot\overline{r}\cdot\cos(\varphi)} + \frac{b}{\sqrt{\overline{r}^2+1-2\cdot\overline{r}\cdot\cos(\varphi)}} \cdot \arctan\frac{\overline{z}-\overline{t}}{\sqrt{\overline{r}^2+1-2\cdot\overline{r}\cdot\cos(\varphi)}} - \frac{a+b\cdot\overline{z}_{wII}(\overline{r},\overline{z},\varphi)}{(\overline{z}-\overline{z}_{wII}(\overline{r},\overline{z},\varphi))^2+\overline{r}^2+1-2\cdot\overline{r}\cdot\cos(\varphi)} - \frac{b}{\sqrt{\overline{r}^2+1-2\cdot\overline{r}\cdot\cos(\varphi)}} \cdot \arctan\frac{\overline{z}-\overline{z}_{wII}(\overline{r},\overline{z},\varphi)}{\sqrt{\overline{r}^2+1-2\cdot\overline{r}\cdot\cos(\varphi)}} \right] \cdot d\varphi$$	$\overline{r} > \left(2\cdot\frac{\overline{z}}{\overline{t}} - 1\right)$ and $\overline{z} > \overline{t}$

Upstream volume

Region	Equation	Border conditionals
II	$$\overline{\Gamma}_w(\overline{r},\overline{z}) = \frac{1}{\pi} \cdot \int_{\varphi_{wt}(\overline{r},\overline{z})}^{\varphi_{wIIn}(\overline{r},\overline{z})} [1-\overline{r}\cdot\cos(\varphi)] \cdot \left[\frac{a+b\cdot\overline{z}_{wIIn}(\overline{r},\overline{z},\varphi)}{(\overline{z}-\overline{z}_{wIIn}(\overline{r},\overline{z},\varphi))^2+\overline{r}^2+1-2\cdot\overline{r}\cdot\cos(\varphi)} + \frac{b}{\sqrt{\overline{r}^2+1-2\cdot\overline{r}\cdot\cos(\varphi)}} \cdot \arctan\frac{\overline{z}-\overline{z}_{wIIn}(\overline{r},\overline{z},\varphi)}{\sqrt{\overline{r}^2+1-2\cdot\overline{r}\cdot\cos(\varphi)}} - \frac{a}{\overline{z}^2+\overline{r}^2+1-2\cdot\overline{r}\cdot\cos(\varphi)} - \frac{b}{\sqrt{\overline{r}^2+1-2\cdot\overline{r}\cdot\cos(\varphi)}} \cdot \arctan\frac{\overline{z}}{\sqrt{\overline{r}^2+1-2\cdot\overline{r}\cdot\cos(\varphi)}} \right] \cdot d\varphi$$ $$+ \frac{1}{\pi} \cdot \int_{\varphi_{wIIn}(\overline{r},\overline{z})}^{\pi} [1-\overline{r}\cdot\cos(\varphi)] \cdot \left[\frac{a+b\cdot\overline{t}}{(\overline{z}-\overline{t})^2+\overline{r}^2+1-2\cdot\overline{r}\cdot\cos(\varphi)} + \frac{b}{\sqrt{\overline{r}^2+1-2\cdot\overline{r}\cdot\cos(\varphi)}} \cdot \arctan\frac{\overline{z}-\overline{t}}{\sqrt{\overline{r}^2+1-2\cdot\overline{r}\cdot\cos(\varphi)}} - \frac{a}{\overline{z}^2+\overline{r}^2+1-2\cdot\overline{r}\cdot\cos(\varphi)} - \frac{b}{\sqrt{\overline{r}^2+1-2\cdot\overline{r}\cdot\cos(\varphi)}} \cdot \arctan\frac{\overline{z}}{\sqrt{\overline{r}^2+1-2\cdot\overline{r}\cdot\cos(\varphi)}} \right] \cdot d\varphi$$	$1 < \overline{r} \le \left(1 - 2\cdot\frac{\overline{z}}{\overline{t}}\right)$ and $\overline{z} < 0$
III	$$\overline{\Gamma}_w(\overline{r},\overline{z}) = \frac{1}{\pi} \cdot \int_{\varphi_{wt}(\overline{r},\overline{z})}^{\pi} [1-\overline{r}\cdot\cos(\varphi)] \cdot \left[\frac{a+b\cdot\overline{z}_{wIIn}(\overline{r},\overline{z},\varphi)}{(\overline{z}-\overline{z}_{wIIn}(\overline{r},\overline{z},\varphi))^2+\overline{r}^2+1-2\cdot\overline{r}\cdot\cos(\varphi)} + \frac{b}{\sqrt{\overline{r}^2+1-2\cdot\overline{r}\cdot\cos(\varphi)}} \cdot \arctan\frac{\overline{z}-\overline{z}_{wIIn}(\overline{r},\overline{z},\varphi)}{\sqrt{\overline{r}^2+1-2\cdot\overline{r}\cdot\cos(\varphi)}} - \frac{a}{\overline{z}^2+\overline{r}^2+1-2\cdot\overline{r}\cdot\cos(\varphi)} - \frac{b}{\sqrt{\overline{r}^2+1-2\cdot\overline{r}\cdot\cos(\varphi)}} \cdot \arctan\frac{\overline{z}}{\sqrt{\overline{r}^2+1-2\cdot\overline{r}\cdot\cos(\varphi)}} \right] \cdot d\varphi$$	$\overline{r} > \left(1 - 2\cdot\frac{\overline{z}}{\overline{t}}\right)$ and $\overline{z} < 0$

Region	Equation	Border conditionals
	Downstream and Interior volumes	
I	$$\bar{n}_o(\bar{r}, \bar{z}) = \frac{1}{2}$$	$\bar{r} \leq 1$ and $\bar{z} = 0$
	$$\bar{n}_o(\bar{r}, \bar{z}) = \frac{\bar{z}}{2 \cdot \pi} \cdot \int_0^\pi \left[\frac{\bar{r} \cdot \cos(\varphi) - \bar{z}^2 - \bar{r}^2}{\left(\bar{r}^2 \cdot \sin(\varphi)^2 + \bar{z}^2\right) \cdot \sqrt{1 - 2 \cdot \bar{r} \cdot \cos(\varphi) + \bar{z}^2 + \bar{r}^2}} + \frac{\sqrt{\bar{z}^2 + \bar{r}^2}}{\bar{r}^2 \cdot \sin(\varphi)^2 + \bar{z}^2} \right] \cdot d\varphi$$	$\bar{r} \leq 1$ and $\bar{z} > 0$
II	$$\bar{n}_o(\bar{r}, \bar{z}) = \frac{\bar{z}}{2 \cdot \pi} \cdot \int_0^{\varphi_{oII}(\bar{r},\bar{z})} \left[\frac{\bar{r} \cdot \bar{r}_{oII}(\bar{r}, \bar{z}, \varphi) \cdot \cos(\varphi) - \bar{z}^2 - \bar{r}^2}{\left(\bar{r}^2 \cdot \sin(\varphi)^2 + \bar{z}^2\right) \cdot \sqrt{\bar{r}_{oII}(\bar{r}, \bar{z}, \varphi)^2 - 2 \cdot \bar{r}_{oII}(\bar{r}, \bar{z}, \varphi) \cdot \bar{r} \cdot \cos(\varphi) + \bar{z}^2 + \bar{r}^2}} + \frac{\sqrt{\bar{z}^2 + \bar{r}^2}}{\bar{r}^2 \cdot \sin(\varphi)^2 + \bar{z}^2} \right] \cdot d\varphi$$ $$+ \frac{\bar{z}}{2 \cdot \pi} \cdot \int_{\varphi_{oII}(\bar{r},\bar{z})}^\pi \left[\frac{\bar{r} \cdot \cos(\varphi) - \bar{z}^2 - \bar{r}^2}{\left(\bar{r}^2 \cdot \sin(\varphi)^2 + \bar{z}^2\right) \cdot \sqrt{1 - 2 \cdot \bar{r} \cdot \cos(\varphi) + \bar{z}^2 + \bar{r}^2}} + \frac{\sqrt{\bar{z}^2 + \bar{r}^2}}{\bar{r}^2 \cdot \sin(\varphi)^2 + \bar{z}^2} \right] \cdot d\varphi$$	$1 < \bar{r} \leq \dfrac{\bar{z}}{t}$ and $\bar{z} > \bar{t}$
IIIa	$$\bar{n}_o(\bar{r}, \bar{z}) = \frac{\bar{z}}{2 \cdot \pi} \cdot \int_{\varphi_{o\max}(\bar{r},\bar{z})}^{\varphi_{oII}(\bar{r},\bar{z})} \left[\frac{\bar{r} \cdot \bar{r}_{oII}(\bar{r}, \bar{z}, \varphi) \cdot \cos(\varphi) - \bar{z}^2 - \bar{r}^2}{\left(\bar{r}^2 \cdot \sin(\varphi)^2 + \bar{z}^2\right) \cdot \sqrt{\bar{r}_{oII}(\bar{r}, \bar{z}, \varphi)^2 - 2 \cdot \bar{r}_{oII}(\bar{r}, \bar{z}, \varphi) \cdot \bar{r} \cdot \cos(\varphi) + \bar{z}^2 + \bar{r}^2}} - \frac{\bar{r} \cdot \bar{r}_{oIII}(\bar{r}, \bar{z}, \varphi) \cdot \cos(\varphi) - \bar{z}^2 - \bar{r}^2}{\left(\bar{r}^2 \cdot \sin(\varphi)^2 + \bar{z}^2\right) \cdot \sqrt{\bar{r}_{oIII}(\bar{r}, \bar{z}, \varphi)^2 - 2 \cdot \bar{r}_{oIII}(\bar{r}, \bar{z}, \varphi) \cdot \bar{r} \cdot \cos(\varphi) + \bar{z}^2 + \bar{r}^2}} \right] \cdot d\varphi$$	$\dfrac{\bar{z}}{t} < \bar{r} \leq \left[\dfrac{\bar{z}}{t} \cdot \sqrt{\left(1 - \dfrac{\bar{t}}{\bar{z}}\right)^2} + 1 \right]$ and $\bar{z} > \bar{t}$
IIIb	$$\bar{n}_o(\bar{r}, \bar{z}) = \frac{\bar{z}}{2 \cdot \pi} \cdot \int_0^{\varphi_{oII}(\bar{r},\bar{z})} \left[\frac{\bar{r} \cdot \cos(\varphi) - \bar{z}^2 - \bar{r}^2}{\left(\bar{r}^2 \cdot \sin(\varphi)^2 + \bar{z}^2\right) \cdot \sqrt{1 - 2 \cdot \bar{r} \cdot \cos(\varphi) + \bar{z}^2 + \bar{r}^2}} - \frac{\bar{r} \cdot \bar{r}_{oIII}(\bar{r}, \bar{z}, \varphi) \cdot \cos(\varphi) - \bar{z}^2 - \bar{r}^2}{\left(\bar{r}^2 \cdot \sin(\varphi)^2 + \bar{z}^2\right) \cdot \sqrt{\bar{r}_{oIII}(\bar{r}, \bar{z}, \varphi)^2 - 2 \cdot \bar{r}_{oIII}(\bar{r}, \bar{z}, \varphi) \cdot \bar{r} \cdot \cos(\varphi) + \bar{z}^2 + \bar{r}^2}} \right] \cdot d\varphi$$	$\left[\dfrac{\bar{z}}{t} \cdot \sqrt{\left(1 - \dfrac{\bar{t}}{\bar{z}}\right)^2} + 1 \right] < \bar{r} \leq \left(2 \cdot \dfrac{\bar{z}}{t} - 1\right)$ and $\bar{z} > \bar{t}$
IV	$$\bar{n}_o(\bar{r}, \bar{z}) = 0$$	$\bar{r} > \left(2 \cdot \dfrac{\bar{z}}{t} - 1\right)$ and $\bar{z} > \bar{t}$
	Upstream volume	
-	$$\bar{n}_o(\bar{r}, \bar{z}) = 1 - \frac{|\bar{z}|}{2 \cdot \pi} \cdot \int_0^\pi \left[\frac{\bar{r} \cdot \cos(\varphi) - \bar{z}^2 - \bar{r}^2}{\left(\bar{r}^2 \cdot \sin(\varphi)^2 + \bar{z}^2\right) \cdot \sqrt{1 - 2 \cdot \bar{r} \cdot \cos(\varphi) + \bar{z}^2 + \bar{r}^2}} + \frac{\sqrt{\bar{z}^2 + \bar{r}^2}}{\bar{r}^2 \cdot \sin(\varphi)^2 + \bar{z}^2} \right] \cdot d\varphi$$	$\bar{z} < 0$

Region	Equation	Border conditionals
I	$\bar{n}_w(\bar{r},\bar{z}) = \dfrac{1}{2\cdot\pi}\displaystyle\int_0^\pi \left[\dfrac{\bar{r}\cdot\cos(\varphi)-1}{\bar{r}^2+1-2\cdot\bar{r}\cdot\cos(\varphi)}\right]\cdot\left[\dfrac{(a+b\cdot\bar{z})\cdot(\bar{z}-\bar{t})+b\cdot(\bar{r}^2+1-2\cdot\bar{r}\cdot\cos(\varphi))}{\sqrt{(\bar{z}-\bar{t})^2+\bar{r}^2+1-2\cdot\bar{r}\cdot\cos(\varphi)}} - \dfrac{(a+b\cdot\bar{z})\cdot\bar{z}+b\cdot(\bar{r}^2+1-2\cdot\bar{r}\cdot\cos(\varphi))}{\sqrt{\bar{z}^2+\bar{r}^2+1-2\cdot\bar{r}\cdot\cos(\varphi)}}\right]\cdot d\varphi$	$\bar{r}\leq 1$

Downstream and Interior volumes

Region	Equation	Border conditionals
II	$\bar{n}_w(\bar{r},\bar{z}) = \dfrac{1}{2\cdot\pi}\displaystyle\int_{\varphi_{wI}(\bar{r},\bar{z})}^{\varphi_{wII}(\bar{r},\bar{z})} \left[\dfrac{\bar{r}\cdot\cos(\phi)-1}{\bar{r}^2+1-2\cdot\bar{r}\cdot\cos(\phi)}\right]\cdot\left\{\dfrac{(a+b\cdot\bar{z})\cdot(\bar{z}-\bar{t})+b\cdot(\bar{r}^2+1-2\cdot\bar{r}\cdot\cos(\varphi))}{\sqrt{(\bar{z}-\bar{t})^2+\bar{r}^2+1-2\cdot\bar{r}\cdot\cos(\varphi)}} - \dfrac{(a+b\cdot\bar{z})\cdot[\bar{z}-\bar{z}_{wII}(\bar{r},\bar{z},\varphi)]+b\cdot(\bar{r}^2+1-2\cdot\bar{r}\cdot\cos(\varphi))}{\sqrt{[\bar{z}-\bar{z}_{wII}(\bar{r},\bar{z},\varphi)]^2+\bar{r}^2+1-2\cdot\bar{r}\cdot\cos(\varphi)}}\right\}\cdot d\varphi$ $+\dfrac{1}{2\cdot\pi}\displaystyle\int_{\varphi_{wII}(\bar{r},\bar{z})}^{\pi}\left[\dfrac{\bar{r}\cdot\cos(\varphi)-1}{\bar{r}^2+1-2\cdot\bar{r}\cdot\cos(\varphi)}\right]\cdot\left[\dfrac{(a+b\cdot\bar{z})\cdot(\bar{z}-\bar{t})+b\cdot(\bar{r}^2+1-2\cdot\bar{r}\cdot\cos(\varphi))}{\sqrt{(\bar{z}-\bar{t})^2+\bar{r}^2+1-2\cdot\bar{r}\cdot\cos(\varphi)}} - \dfrac{(a+b\cdot\bar{z})\cdot\bar{z}+b\cdot(\bar{r}^2+1-2\cdot\bar{r}\cdot\cos(\varphi))}{\sqrt{\bar{z}^2+\bar{r}^2+1-2\cdot\bar{r}\cdot\cos(\varphi)}}\right]\cdot d\varphi$	$1<\bar{r}\leq\left(2\cdot\dfrac{\bar{z}}{\bar{t}}-1\right)$ and $\bar{z}>\bar{t}$
III	$\bar{n}_w(\bar{r},\bar{z}) = \dfrac{1}{2\cdot\pi}\displaystyle\int_{\varphi_{wt}(\bar{r},\bar{z})}^{\pi}\left[\dfrac{\bar{r}\cdot\cos(\varphi)-1}{\bar{r}^2+1-2\cdot\bar{r}\cdot\cos(\varphi)}\right]\cdot\left[\dfrac{(a+b\cdot\bar{z})\cdot(\bar{z}-\bar{t})+b\cdot(\bar{r}^2+1-2\cdot\bar{r}\cdot\cos(\varphi))}{\sqrt{(\bar{z}-\bar{t})^2+\bar{r}^2+1-2\cdot\bar{r}\cdot\cos(\varphi)}} - \dfrac{(a+b\cdot\bar{z})\cdot[\bar{z}-\bar{z}_{wII}(\bar{r},\bar{z},\varphi)]+b\cdot(\bar{r}^2+1-2\cdot\bar{r}\cdot\cos(\varphi))}{\sqrt{[\bar{z}-\bar{z}_{wII}(\bar{r},\bar{z},\varphi)]^2+\bar{r}^2+1-2\cdot\bar{r}\cdot\cos(\varphi)}}\right]\cdot d\varphi$	$\bar{r}>\left(2\cdot\dfrac{\bar{z}}{\bar{t}}-1\right)$ and $\bar{z}>\bar{t}$

Upstream volume

Region	Equation	Border conditionals
II	$\bar{n}_w(\bar{r},\bar{z}) = \dfrac{1}{2\cdot\pi}\displaystyle\int_{\varphi_{wt}(\bar{r},\bar{z})}^{\varphi_{wIIn}(\bar{r},\bar{z})}\left[\dfrac{\bar{r}\cdot\cos(\varphi)-1}{\bar{r}^2+1-2\cdot\bar{r}\cdot\cos(\varphi)}\right]\cdot\left\{\dfrac{(a+b\cdot\bar{z})\cdot[\bar{z}-\bar{z}_{wIIn}(\bar{r},\bar{z},\varphi)]+b\cdot(\bar{r}^2+1-2\cdot\bar{r}\cdot\cos(\varphi))}{\sqrt{[\bar{z}-\bar{z}_{wIIn}(\bar{r},\bar{z},\varphi)]^2+\bar{r}^2+1-2\cdot\bar{r}\cdot\cos(\varphi)}} - \dfrac{(a+b\cdot\bar{z})\cdot\bar{z}+b\cdot(\bar{r}^2+1-2\cdot\bar{r}\cdot\cos(\varphi))}{\sqrt{\bar{z}^2+\bar{r}^2+1-2\cdot\bar{r}\cdot\cos(\varphi)}}\right\}\cdot d\varphi$ $+\dfrac{1}{2\cdot\pi}\displaystyle\int_{\varphi_{wIIn}(\bar{r},\bar{z})}^{\pi}\left[\dfrac{\bar{r}\cdot\cos(\varphi)-1}{\bar{r}^2+1-2\cdot\bar{r}\cdot\cos(\varphi)}\right]\cdot\left[\dfrac{(a+b\cdot\bar{z})\cdot(\bar{z}-\bar{t})+b\cdot(\bar{r}^2+1-2\cdot\bar{r}\cdot\cos(\varphi))}{\sqrt{(\bar{z}-\bar{t})^2+\bar{r}^2+1-2\cdot\bar{r}\cdot\cos(\varphi)}} - \dfrac{(a+b\cdot\bar{z})\cdot\bar{z}+b\cdot(\bar{r}^2+1-2\cdot\bar{r}\cdot\cos(\varphi))}{\sqrt{\bar{z}^2+\bar{r}^2+1-2\cdot\bar{r}\cdot\cos(\varphi)}}\right]\cdot d\varphi$	$1<\bar{r}\leq\left(1-2\cdot\dfrac{\bar{z}}{\bar{t}}\right)$ and $\bar{z}<0$
III	$\bar{n}_w(\bar{r},\bar{z}) = \dfrac{1}{2\cdot\pi}\displaystyle\int_{\varphi_{wt}(\bar{r},\bar{z})}^{\pi}\left[\dfrac{\bar{r}\cdot\cos(\varphi)-1}{\bar{r}^2+1-2\cdot\bar{r}\cdot\cos(\varphi)}\right]\cdot\left[\dfrac{(a+b\cdot\bar{z})\cdot[\bar{z}-\bar{z}_{wIIn}(\bar{r},\bar{z},\varphi)]+b\cdot(\bar{r}^2+1-2\cdot\bar{r}\cdot\cos(\varphi))}{\sqrt{[\bar{z}-\bar{z}_{wIIn}(\bar{r},\bar{z},\varphi)]^2+\bar{r}^2+1-2\cdot\bar{r}\cdot\cos(\varphi)}} - \dfrac{(a+b\cdot\bar{z})\cdot(\bar{z}-\bar{t})+b\cdot(\bar{r}^2+1-2\cdot\bar{r}\cdot\cos(\varphi))}{\sqrt{(\bar{z}-\bar{t})^2+\bar{r}^2+1-2\cdot\bar{r}\cdot\cos(\varphi)}}\right]\cdot d\varphi$	$\bar{r}>\left(1-2\cdot\dfrac{\bar{z}}{\bar{t}}\right)$ and $\bar{z}<0$

TABLE 5.—VARIABLE LIMITS OF INTEGRATION USED IN TABLES 1 TO 4

Table use	Type	Limit equation
Tables 1 and 3	Radial	$$\bar{r}_{oII}(\bar{r},\bar{z},\varphi) = \frac{-\dfrac{\bar{t}\cdot\bar{r}}{\bar{z}}\cdot\cos(\varphi) + \sqrt{1 - \left(\dfrac{\bar{t}\cdot\bar{r}}{\bar{z}}\right)^2 \cdot \sin(\varphi)^2}}{1 - \dfrac{\bar{t}}{\bar{z}}}$$
		$$\bar{r}_{oIII}(\bar{r},\bar{z},\varphi) = \frac{-\dfrac{\bar{t}\cdot\bar{r}}{\bar{z}}\cdot\cos(\varphi) - \sqrt{1 - \left(\dfrac{\bar{t}\cdot\bar{r}}{\bar{z}}\right)^2 \cdot \sin(\varphi)^2}}{1 - \dfrac{\bar{t}}{\bar{z}}}$$
	Angular	$$\varphi_{oII}(\bar{r},\bar{z}) = \arccos\left[\frac{1 - \left(1 - \dfrac{\bar{t}}{\bar{z}}\right)^2 - \left(\dfrac{\bar{t}\cdot\bar{r}}{\bar{z}}\right)^2}{2\cdot\dfrac{\bar{t}\cdot\bar{r}}{\bar{z}}\cdot\left(1 - \dfrac{\bar{t}}{\bar{z}}\right)}\right]$$
		$$\varphi_{o\max}(\bar{r},\bar{z}) = \pi - \arcsin\left(\frac{\bar{z}}{\bar{t}\cdot\bar{r}}\right)$$
Tables 2 and 4	Axial	$$\bar{z}_{wII}(\bar{r},\bar{z},\varphi) = \frac{\bar{r}^2\cdot\bar{t} + \bar{t} - 2\cdot\bar{z} - 2\cdot\bar{r}\cdot(\bar{t}-\bar{z})\cdot\cos(\varphi)}{\bar{r}^2 - 1}$$
		$$\bar{z}_{wIIn}(\bar{r},\bar{z},\phi) = 2\cdot\bar{z}\cdot\frac{1 - \bar{r}\cdot\cos(\phi)}{1 - \bar{r}^2}$$
	Angular	$$\varphi_{wII}(\bar{r},\bar{z}) = \arccos\left[\frac{\bar{r}^2 + 1 - 2\cdot\dfrac{\bar{z}}{\bar{t}}}{2\cdot\bar{r}\cdot\left(1 - \dfrac{\bar{z}}{\bar{t}}\right)}\right]$$
		$$\varphi_{wIIn}(\bar{r},\bar{z}) = \arccos\left[\frac{\bar{r}^2 - 1 + 2\cdot\dfrac{\bar{z}}{\bar{t}}}{2\cdot\bar{r}\cdot\dfrac{\bar{z}}{\bar{t}}}\right]$$
		$$\varphi_{wt}(\bar{r},\bar{z}) = \arccos\left(\frac{1}{\bar{r}}\right)$$

V. Far-field Equations Using Clausing's Angular Distribution Equation

A commonly accepted far-field expression will be presented here for later comparisons with the more rigorously developed equations above. Clausing was the first to develop a far-field expression for the angular distribution of particles downstream of a cylindrical aperture (Ref. 3). His equation assumes that the aperture is a point source and that the flux of particles from the walls of the aperture is linear as a function of axial thickness. The angular distribution of particles downstream of a cylindrical aperture, $T(\alpha)$, in the far-field is given by (Refs. 4 and 5):

$$
T(\alpha) =
\begin{cases}
1 - \left\{ \dfrac{2}{\pi} \cdot (1-\kappa) \cdot \left[\arcsin\left(\dfrac{\bar{t} \cdot \tan(\alpha)}{2} \right) + \dfrac{\bar{t} \cdot \tan(\alpha)}{2} \cdot \sqrt{1 - \left(\dfrac{\bar{t} \cdot \tan(\alpha)}{2} \right)^2} \right] \right\} + \dfrac{4}{3 \cdot \pi} \cdot (1 - 2 \cdot \kappa) \cdot \dfrac{1 - \left[1 - \left(\dfrac{\bar{t} \cdot \tan(\alpha)}{2} \right)^2 \right]^{\frac{3}{2}}}{\dfrac{\bar{t} \cdot \tan(\alpha)}{2}} & \text{if } \alpha \leq \arctan\left(\dfrac{2}{\bar{t}} \right) \\[4ex]
\text{and} \\[2ex]
\kappa + \dfrac{4}{3 \cdot \pi} \cdot \dfrac{1 - 2 \cdot \kappa}{\dfrac{\bar{t} \cdot \tan(\alpha)}{2}} & \text{if } \alpha > \arctan\left(\dfrac{2}{\bar{t}} \right)
\end{cases}
\tag{55}
$$

where:

$$
\kappa = \frac{\sqrt{\bar{t}^2 + 4} - \bar{t}}{2 + \dfrac{4}{\sqrt{\bar{t}^2 + 4}}}
\tag{56}
$$

Figure 15 shows the geometry for a single aperture that is treated as a point source. It can easily be shown that:

$$
L = \sqrt{r^2 + (z-t)^2}
\tag{57}
$$

and:

$$
\cos(\alpha) = \cos(\delta) = \frac{z-t}{\sqrt{r^2 + (z-t)^2}}
\tag{58}
$$

Equations (57) and (58), along with $T(\alpha)$, can be substituted into Equations (5) and (9) to determine the downstream particle flux and density from a cylindrical aperture in the far-field. Note that all variables are independent of dA_o because a point source is assumed, so that integral reduces to $\pi \cdot R^2$. The resulting equation for the far-field flux, Γ_{far}, is given in non-dimensional form by:

$$
\overline{\Gamma}_{far}(\bar{r}, \bar{z}) = T\left[\arccos\left(\frac{\bar{z} - \bar{t}}{\sqrt{\bar{r}^2 + (\bar{z} - \bar{t})^2}} \right) \right] \cdot \frac{(\bar{z} - \bar{t})^2}{\left(\bar{r}^2 + (\bar{z} - \bar{t})^2 \right)^2}
\tag{59}
$$

while the far-field density, n_{far}, is given in non-dimensional by:

$$
\bar{n}_{far}(\bar{r}, \bar{z}) = \frac{1}{4} \cdot T\left[\arccos\left(\frac{\bar{z} - \bar{t}}{\sqrt{\bar{r}^2 + (\bar{z} - \bar{t})^2}} \right) \right] \cdot \frac{\bar{z} - \bar{t}}{\left(\bar{r}^2 + (\bar{z} - \bar{t})^2 \right)^{\frac{3}{2}}}
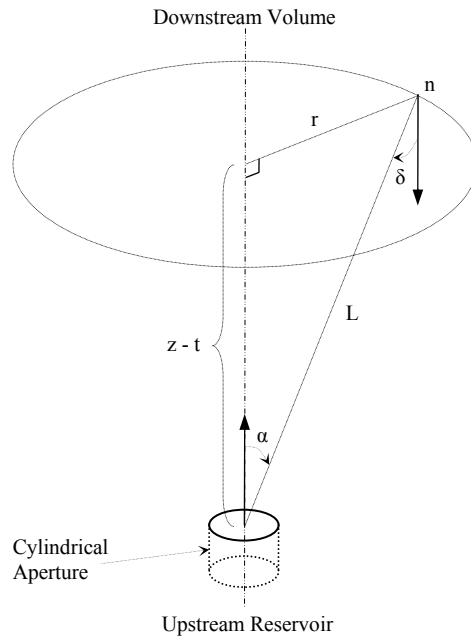\tag{60}
$$

Figure 15.—Geometry for determining downstream
axial flux and density in the far-field.

The transmission probability of particles through a cylindrical aperture can also be determined by integrating Clausing's angular distribution function over all azimuthal and polar angles and dividing by that of a diffuse distribution. It can be shown that this probability, P_{far}, is given by (Ref. 5):

$$P_{far} = \frac{\int_0^{2\cdot\pi}\int_0^{\frac{\pi}{2}} T(\alpha)\cdot\cos(\alpha)\cdot\sin(\alpha)\cdot d\alpha\cdot d\varphi}{\int_0^{2\cdot\pi}\int_0^{\frac{\pi}{2}}\cos(\alpha)\cdot\sin(\alpha)\cdot d\alpha\cdot d\varphi} = 2\cdot\int_0^{\frac{\pi}{2}} T(\alpha)\cdot\cos(\alpha)\cdot\sin(\alpha)\cdot d\alpha \qquad (61)$$

VI. Results

The following sections will present the results of the particle flux and density equations developed in this study. First, an assessment of the linear wall flux distribution assumption will be made. Then, the axial flux and density equations from this study will be applied to a cylindrical aperture and compared to those of Clausing's far-field expression to accomplish the following: 1) the commonly accepted far-field expression will be used to verify the rigorously developed equations in the far-field; and 2) the rigorously developed equations will be used to determine the efficacy of the far-field expression in the near-field. A typical ion thruster aperture thickness-to-radius ratio of 1.25 will be used throughout. Finally, the axial flux and density equations will be verified using three different methods.

A. Assessment of Linear Wall Flux Assumption and Transmission Probabilities

As was shown earlier in Figures 3 and 4, the linear axial wall flux distribution assumption of Equation (14) accurately models the true distribution over a range of aperture thickness-to-radius ratios. However, it would be useful to determine a figure of merit for setting the maximum thickness-to-radius ratio that can utilize this assumption. One figure of merit is the particle transmission probability. Figure 16 shows the error between the true transmission probabilities (i.e., those determined numerically per Reference 7 with an error of ≤0.25 percent) and those determined with Equation (54), which assumes a linear distribution assumption. The figure shows that transmission probability errors with a linear wall flux distribution assumption are 4 percent for thickness-to-radius ratios ≤16. However, in state-of-the-art ion thruster perforated grids, the thickness-to-radius ratio is within 1.25, so the transmission probability error would be <0.1 percent.

Verifying the linear distribution assumption as the cause for this error is essential for assessing its impact on axial flux and density calculations. To better understand the cause of the transmission probability errors, Figure 17 plots the transmission probability of Equation (54) as a function of axial location for a thickness-to-radius ratio of 32. This thickness-to-radius ratio was selected because these errors increase at larger ratios. The transmission probabilities should be constant throughout the axial direction in Figure 17. However, the figure shows that the probability is not constant within the aperture. So, the transmission probability can be in error by as much as 11 percent for this thickness-to-radius ratio. It can be shown that this disparity generally increases for larger thickness-to-radius ratios. Also shown in Figure 17 is the transmission probability when the linear wall flux distribution assumption is replaced with a 5th order polynomial curve fit equation. The polynomial curve fit equation produces a nearly constant transmission probability as a function of axial location whose average value is nearly identical to the true transmission probability. This is significant, because the flux difference between the true and linear distributions never exceeded 1 percent of Γ_o, and yet the impact on transmission probability was a nearly 7 percent error.
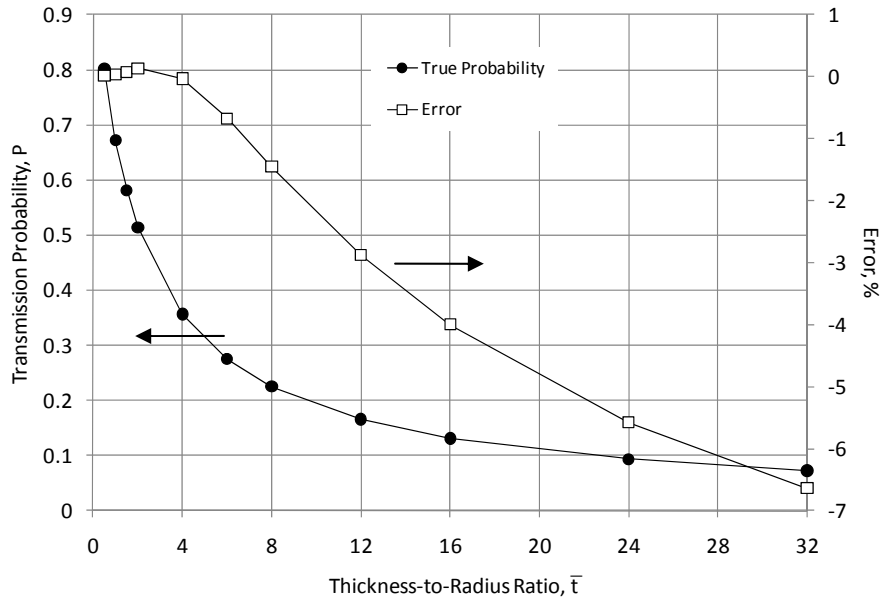

Figure 16.—True transmission probability as a function of aperture thickness-to-radius ratio and the error between the true probability and that assuming a linear wall flux distribution.
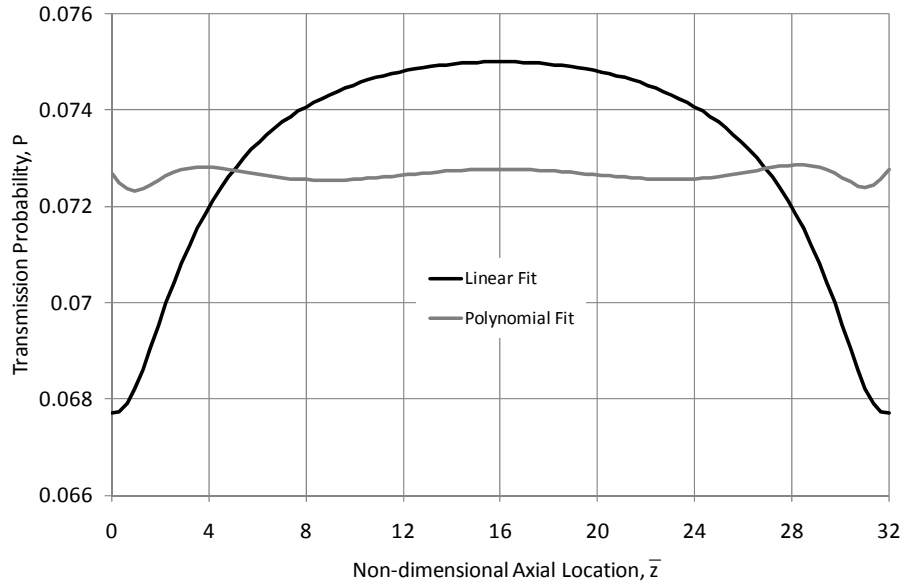
Figure 17.—Transmission probability with linear and polynomial curve fits to the
actual wall flux distribution for a thickness-to-radius ratio of 32.

Because the transmission probability is the integral of the axial flux per Equation (54), the errors plotted in Figure 16 would roughly represent the errors expected for flux, and therefore density, calculations. This assertion was checked for a thickness-to-radius ratio of 32. While the maximum transmission probability error was about 7 percent, the maximum flux error was within 8 percent. So, if a maximum acceptable flux and density error is 4 percent, a linear wall flux distribution assumption can be used for thickness-to-radius ratios ≤16 according to Figure 16.

B. Particle Flux and Density Surrounding a Cylindrical Aperture

1. Near-field Results

The axial flux surrounding a cylindrical aperture with a thickness-to-radius ratio of 1.25 is shown in Figure 18. The plot was determined with Equation (26) and the equations from Tables 1, 2, and 5. As expected, the axial flux decreases rapidly further from the aperture in the upstream, downstream, and radial directions. This is because the flux tends to be equal in all directions upstream of the aperture and the flow expands rapidly downstream of the aperture. It is only within the cylindrical aperture that the aperture and its walls align the flux of the particle flow in the axial direction. It is interesting to note that there is symmetry in the axial direction about $z = t/2$.

Figure 19 shows the contributions of the reservoir and aperture walls to the surrounding axial flux. As expected, the non-dimensional axial flux from the reservoir is 1 (or the reservoir flux, Γ_o) at the aperture inlet plane and this decreases rapidly as the flow expands in all downstream directions. The wall's contribution produces a net negative (i.e., upstream) axial flux near the aperture inlet because of upstream particle reflections from the aperture walls.

The particle density surrounding a cylindrical aperture with a thickness-to-radius ratio of 1.25 is shown in Figure 20. The plot was determined with Equation (29) and the equations from Tables 3 to 5. Far upstream from the aperture inlet, the non-dimensional particle density is constant and equal to 1 (or the reservoir density, n_o). However, closer to the aperture inlet, the figure shows a depleted density zone. This depletion zone is caused by particles escaping through the aperture. The figure also shows that the density drops rapidly from the upstream to downstream regions and through the aperture. Figure 21 shows only the particle density downstream of the aperture. The particle density drops rapidly as particles expand into vacuum, dropping to less than 10 percent of the upstream density within 1 aperture radius of the downstream surface.
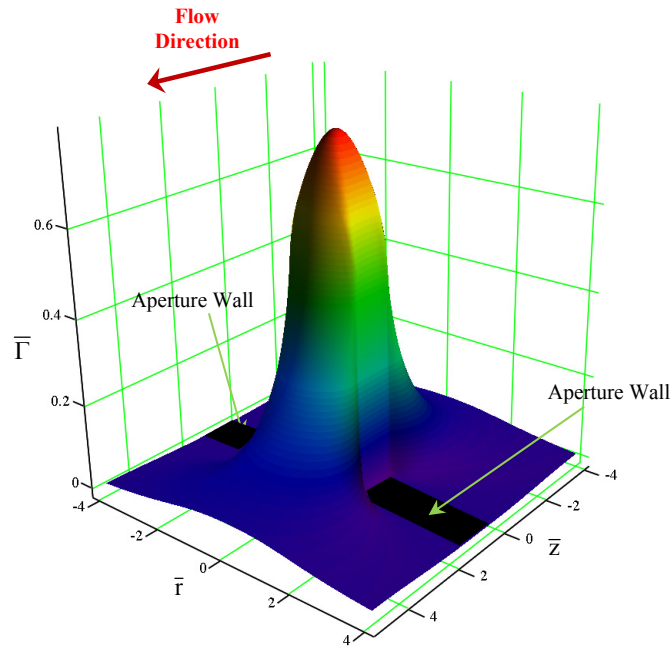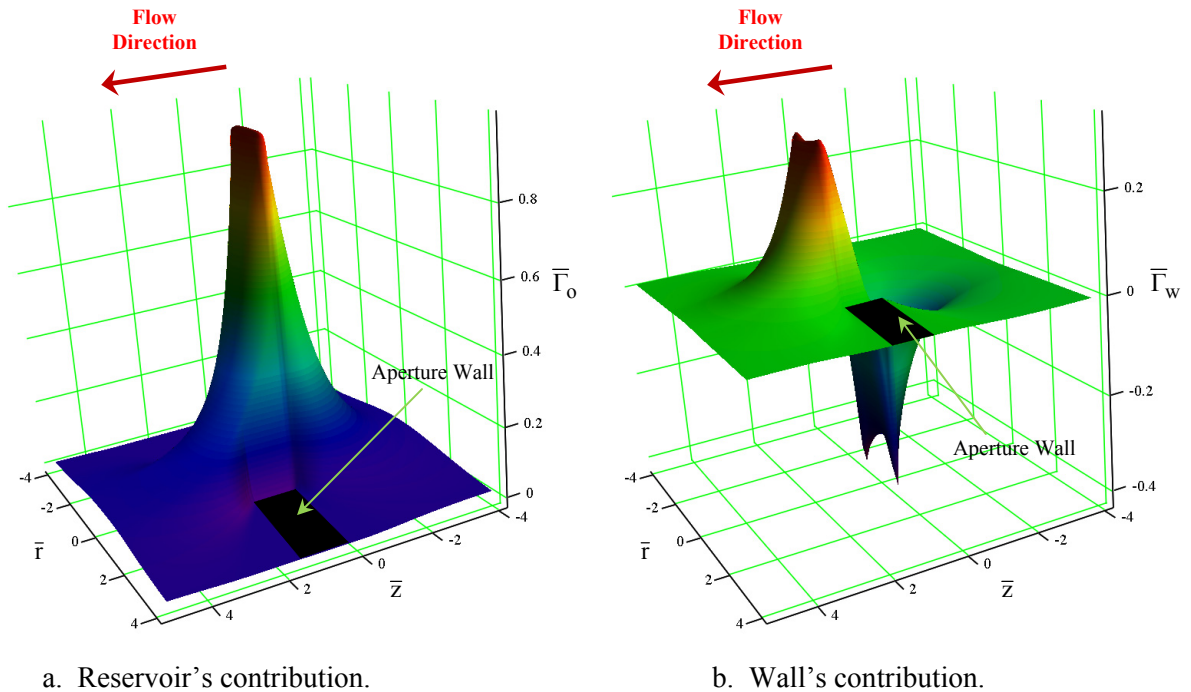
Figure 18.—Axial particle flux surrounding a cylindrical aperture with a thickness-to-radius ratio of 1.25.

a. Reservoir's contribution.

b. Wall's contribution.

Figure 19.—The reservoir's and wall's contributions to the axial particle flux surrounding a cylindrical aperture with a thickness-to-radius ratio of 1.25.
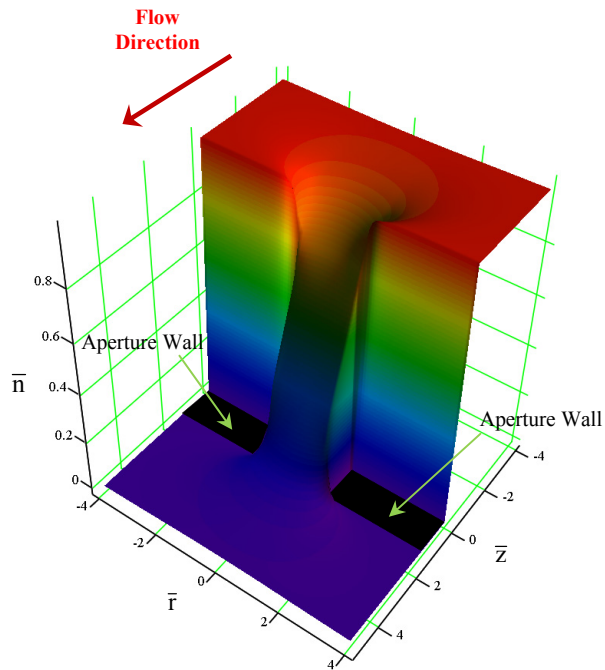
Figure 20.—Particle density surrounding a cylindrical aperture with a thickness-to-radius ratio of 1.25.
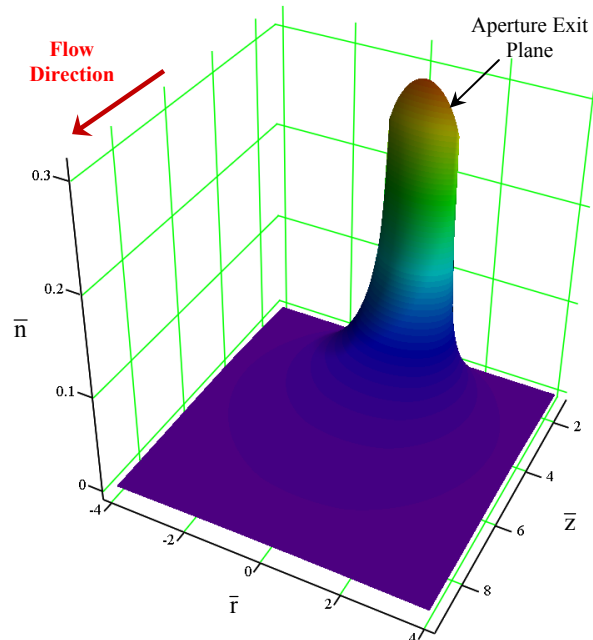

Figure 21.—Particle density downstream of a cylindrical aperture exit plane with a thickness-to-radius ratio of 1.25.

2. Far-field Results and Comparisons with Clausing's Far-field Expression

The far-field particle flux and density equations (i.e., Eqs. (59) and (60), respectively) that utilize Clausing's angular distribution function are compared to that calculated with Equations (26) and (29), respectively, and the equations of Tables 1 to 5 in Figures 22 and 23. Here, the axial flux and density were determined at fixed radial distances from the downstream center of the aperture from 2 to 60 radii while the angle was varied (i.e., a spherical coordinate system was used) to determine angular distributions. The figures illustrate that at increasing distances from the aperture, the far-field angular distribution becomes equal to that of the Equations (26) and (29). The figures also show that the worst-case error in the far-field equation occurs along the axial centerline of the aperture.
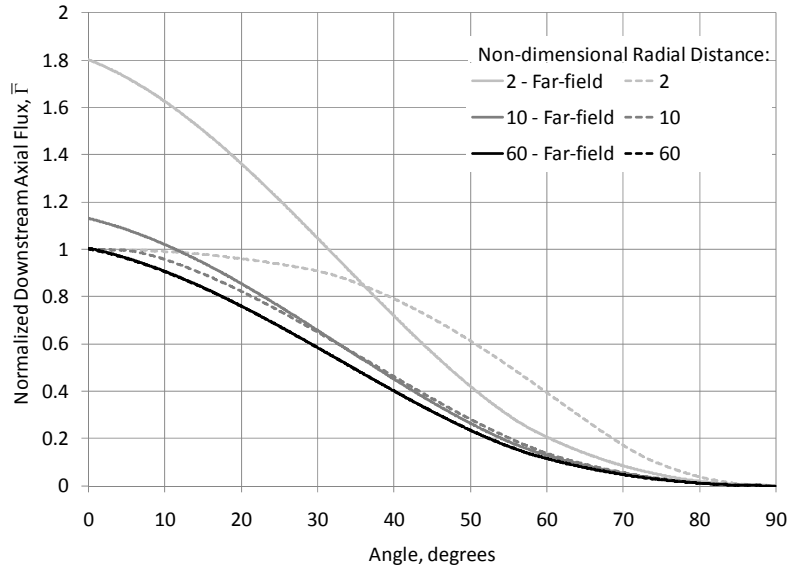
Figure 22.—Normalized axial flux angular distributions for a variety of radial distances in a spherical coordinate system. The aperture thickness-to-radius is 1.25. Solid lines were determined from Equation (59) and dashed lines from Equation (26) and Tables 1, 2, and 5.
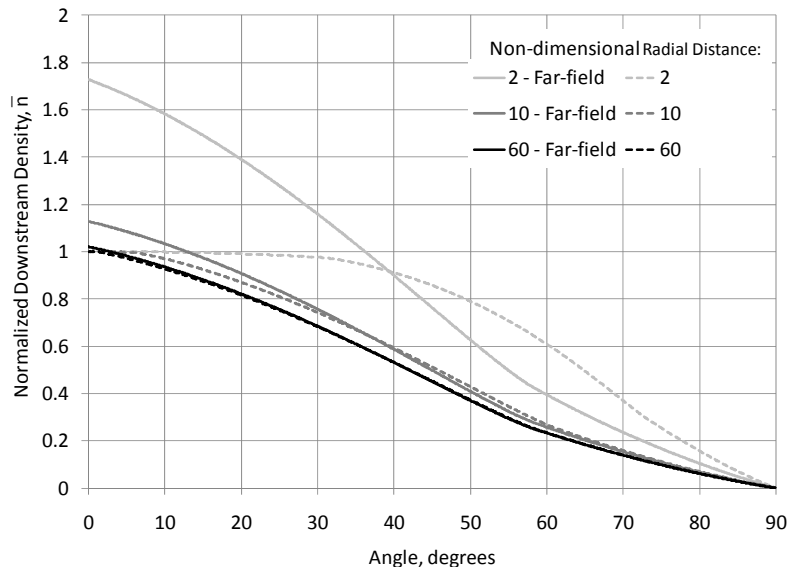

Figure 23.—Normalized density angular distributions for a variety of radial distances in a spherical coordinate system. The aperture thickness-to-radius is 1.25. Solid lines were determined from Equation (60) and dashed lines from Equation (29) and Tables 3 to 5.

Because Equations (26) and (29) along with the equations of Tables 1 to 5 represent a rigorous solution for downstream particle flux and density, respectively, the far-field flux and density equations were compared to them in Figures 24 and 25 to determine the error as a function of radial distance from the downstream aperture center at various angles. The figures show that both far-field equation errors reduce to about 5 percent at about 25 aperture radii downstream for the 0° case, but within 9 aperture radii for the remaining angles. These figures demonstrate that the far-field equations will produce accurate results at >9 aperture radii downstream of a cylindrical aperture with a thickness-to-radius ratio of 1.25.
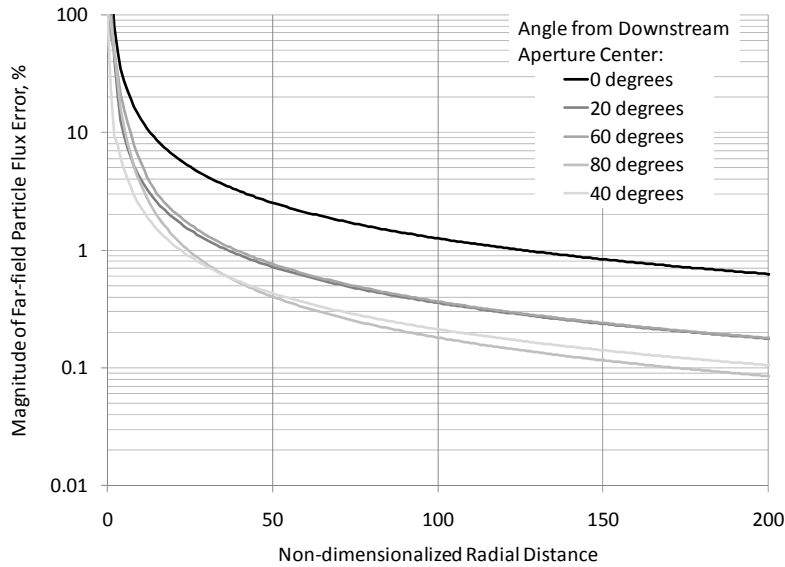
Figure 24.—Far-field flux error as a function of radial distance at various angles in a spherical coordinate system. The aperture thickness-to-radius is 1.25. Error is equal to 100·|Equations (26) to (59)|/Equation (26).
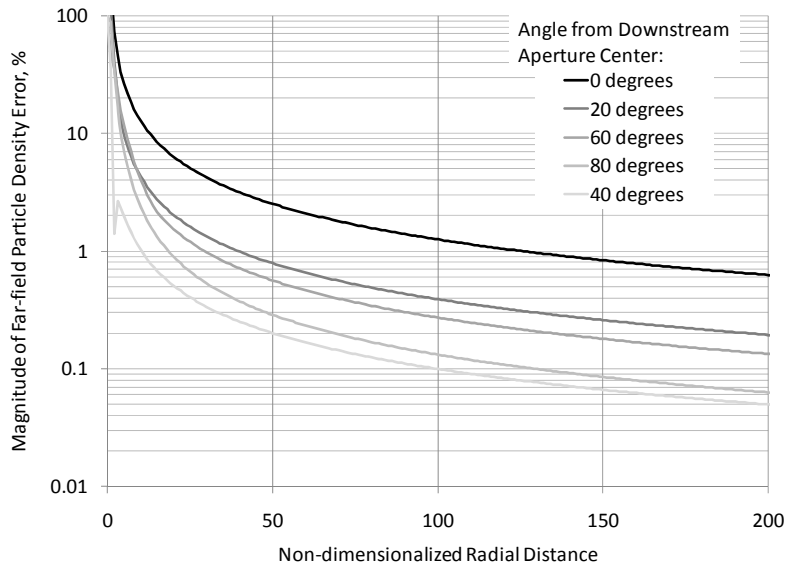
Figure 25.—Far-field density error as a function of radial distance at various angles in a spherical coordinate system. The aperture thickness-to-radius is 1.25. Error is equal to 100·|Equations (29) to (60)|/Equation (29).

C. Verification of Equations—Clausing's Far-field Expression and Conservation of Mass

The equations determined in this study for the axial flux and density surrounding a cylindrical aperture were verified using three methods. First, comparisons were made to a commonly accepted expression determined by Clausing (Refs. 3 and 4). This was done in the prior section for both the axial flux and density in Figures 22 to 25. Results showed that maximum differences were within 5 percent at >25 aperture radii downstream and that these differences decreased with increasing distance. So, the equations determined in this study compare favorably to that determined by Clausing in the far-field downstream volume.

A second method was to compare the transmission probabilities of the far-field expression (i.e., Eq. (61)) to that of the more rigorous Equation (54). Because both equations were determined assuming a linear wall flux distribution, both equations should yield the same transmission probabilities. Comparisons were made over a broad range of thickness-to-radius ratios, and Equations (54) and (61) were found produce nearly identical results.

A third method was to verify conservation of mass throughout the axial direction. For mass to be conserved, the total axial particle flow rate must be constant (i.e., independent of axial location, z). The total axial particle flow rate is determined by integrating the axial flux radially at a given location. Note that this is merely the transmission probability multiplied by the particle flux at the aperture inlet, which is a constant. Therefore, merely demonstrating a constant transmission probability along z with Equation (54) would assure that mass was conserved. This was done over a range of thickness-to-radius ratios and axial locations, and transmission probabilities were found to be constant, so mass was conserved.

VII. Conclusions

The equations for rigorously calculating the particle flux and density surrounding a cylindrical aperture in the free molecular flow regime were developed and presented. Previous work did not provide accurate near-field determinations of particle flux and density. The fundamental equations for particle flux and density from a reservoir and a diffusely reflecting wall were developed and presented. Assumptions included, in part, a Maxwell-Boltzmann speed distribution, equal particle and wall temperatures, and a linear flux distribution from the cylindrical aperture walls. With this information, the equations for axial flux and density surrounding a cylindrical aperture were developed. The cylindrical aperture was divided into three volumes (i.e., upstream reservoir, interior, and downstream), and the upstream and downstream volumes were further divided into multiple regions to rigorously determine axial flux and density. After the base equations for flux and density were determined, the limits of integration were developed for all volumes and regions. The complete set of flux and density equations was presented along with an equation for the transmission probability. Finally, a commonly accepted far-field angular distribution expression was used to develop far-field flux, density, and transmission probabilities for comparisons.

An assessment of the linear wall flux distribution assumption showed that a thickness-to-radius ratio of 16 would produce an axial flux and density error of 4 percent and that this error decreased with decreasing thickness-to-radius ratios. The axial flux and density surrounding a cylindrical aperture with a thickness-to-radius ratio of 1.25 was presented. The axial flux was found to be axially symmetric about 1/2 of the aperture plate thickness. Both axial flux and density were found to decrease rapidly downstream as the flow exhausting from the aperture expanded into vacuum.

Finally, the equations determined in this study were verified using three methods. Comparisons to a commonly accepted far-field expression showed that maximum differences were within 5 percent at 25 aperture radii downstream and that these differences decreased with increasing distance. The transmission probabilities of the far-field expression were also nearly identical to those determined from this study. Finally, conservation of mass was confirmed in the axial direction.

References

1. Kaufman, H.R., "Technology of Electron-bombardment Thrusters," <u>Advances in Electronics and Electron Physics</u>, vol. 36, Academic Press, New York, 1974, pp. 265–373.
2. Goebel, D.M. and Katz, I., <u>Fundamentals of Electric Propulsion: Ion and Hall Thrusters</u>, John Wiley and Sons, Inc, Hoboken NJ, 2008.
3. Soulas, G.C., "Modeling Neutral Densities Downstream of a Gridded Ion Thruster," 46th AIAA/ASME/SAE/ASEE Joint Propulsion Conference & Exhibit, AIAA Paper 2010-6699, July 2010.
4. Clausing, P., "The Formation of Beams in Molecular Streaming," Z. Physik, vol. 66, pp. 471–476, 1930.

5. Dayton, B.B., "Gas Flow Patterns at Entrance and Exit of Cylindrical Tubes," <u>National Symposium on Vacuum Technology Transactions</u>, Pergamon Press, New York, 1956, pp. 5–11.

6. Reynolds, T.W. and Richley, E.A., "Free-molecule Flow and Surface Diffusion Thruster Slots and Tubes," NASA Technical Report R-255, April 1967.

7. Richley, E.A. and Reynolds, T.W. "Numerical Solutions of Free-molecule Flow in Converging and Diverging Tubes and Slots," NASA Technical Note D-2330, June 1964.

8. Robertson, S.J., "A Study of Density Variations in Free Molecular Flow Through Cylindrical Ducts due to Accommodation Coefficients," NASA Technical Memorandum TM X-53516, November 1964.

9. Bird, G.A., <u>Molecular Gas Dynamics and the Direct Simulation of Gas Flows</u>, Oxford University Press, Oxford, 1996.

10. Beijerinck, H.C.W., Stevens, P.J.M., and Verster, N.F., "Monte-Carlo Calculation of Molecular Flow Through a Cylindrical Channel," *Physica*, vol. 83c, 1976, pp. 209–219.

11. Gombosi, T.I., <u>Gas Kinetic Theory</u>, Cambridge University Press, Cambridge, 1994, pp. 18–35.

12. Clausing, P., "The Flow of Highly Rarefied Gases Through Tubes of Arbitrary Length," *Ann. Physik*, vol. 5, no. 12, 1932, p. 961.

13. Narasimha, R., "Orifice Flow at High Knudsen Numbers," *Journal of Fluid Mechanics*, vol. 10, no. 3, 1961, pp. 371–384.

1. REPORT DATE *(DD-MM-YYYY)* 01-03-2011	**2. REPORT TYPE** Technical Memorandum	**3. DATES COVERED** *(From - To)*
4. TITLE AND SUBTITLE Gas Flux and Density Surrounding a Cylindrical Aperture in the Free Molecular Flow Regime		**5a. CONTRACT NUMBER**
		5b. GRANT NUMBER
		5c. PROGRAM ELEMENT NUMBER
6. AUTHOR(S) Soulas, George, C.		**5d. PROJECT NUMBER**
		5e. TASK NUMBER
		5f. WORK UNIT NUMBER WBS 346620.04.08.02.01.01
7. PERFORMING ORGANIZATION NAME(S) AND ADDRESS(ES) National Aeronautics and Space Administration John H. Glenn Research Center at Lewis Field Cleveland, Ohio 44135-3191		**8. PERFORMING ORGANIZATION REPORT NUMBER** E-17598
9. SPONSORING/MONITORING AGENCY NAME(S) AND ADDRESS(ES) National Aeronautics and Space Administration Washington, DC 20546-0001		**10. SPONSORING/MONITOR'S ACRONYM(S)** NASA
		11. SPONSORING/MONITORING REPORT NUMBER NASA/TM-2011-216970

12. DISTRIBUTION/AVAILABILITY STATEMENT Unclassified-Unlimited Subject Category: 20 Available electronically at http://www.sti.nasa.gov This publication is available from the NASA Center for AeroSpace Information, 443-757-5802

13. SUPPLEMENTARY NOTES

14. ABSTRACT
The equations for rigorously calculating the particle flux and density surrounding a cylindrical aperture in the free molecular flow regime are developed and presented. The fundamental equations for particle flux and density from a reservoir and a diffusely reflecting surface will initially be developed. Assumptions will include a Maxwell-Boltzmann speed distribution, equal particle and wall temperatures, and a linear flux distribution along the cylindrical aperture walls. With this information, the equations for axial flux and density surrounding a cylindrical aperture will be developed. The cylindrical aperture will be divided into multiple volumes and regions to rigorously determine the surrounding axial flux and density, and appropriate limits of integration will be determined. The results of these equations will then be evaluated. The linear wall flux distribution assumption will be assessed. The axial flux and density surrounding a cylindrical aperture with a thickness-to-radius ratio of 1.25 will be presented. Finally, the equations determined in this study will be verified using multiple methods.

15. SUBJECT TERMS Ion thruster; Ion engine; Free molecular flow; Density; Flux

16. SECURITY CLASSIFICATION OF:			**17. LIMITATION OF ABSTRACT**	**18. NUMBER OF PAGES**	**19a. NAME OF RESPONSIBLE PERSON** STI Help Desk (email:help@sti.nasa.gov)
a. REPORT U	**b. ABSTRACT** U	**c. THIS PAGE** U	UU	40	**19b. TELEPHONE NUMBER** *(include area code)* 443-757-5802